PCCP

ROYAL SOCIETY OF CHEMISTRY

PAPER

View Article Online
View Journal | View Issue

Cite this: *Phys. Chem. Chem. Phys.*, 2023, **25**, 6636

Origin of anomalously stabilizing ice layers on methane gas hydrates near rock surface

Yang Li, *[ab] Robert W. Corkery,[cd] Sol Carretero-Palacios, [e] Kristian Berland, [f] Victoria Esteso, [gn] Johannes Fiedler, [hi] Kimball A. Milton, *[j] Iver Brevik*[k] and Mathias Boström *[lm]

Received 19th October 2022,
Accepted 22nd December 2022

DOI: 10.1039/d2cp04883c

rsc.li/pccp

Gas hydrates (GHs) in water close to freezing temperatures can be stabilised *via* the formation of ice layers. In a recent work [Boström *et al.*, *Astron. Astrophys.*, **A54**, 650, 2021], it was found that a surface region with partial gas dilution could be essential for obtaining nano- to micron-sized anomalously stabilizing ice layers. In this paper, it is demonstrated that the Casimir–Lifshitz free energy in multi-layer systems could induce thinner, but more stable, ice layers in cavities than those found for gas hydrates in a large reservoir of cold water. The thickness and stability of such ice layers in a pore filled with cold water could influence the leakage of gas molecules. Additional contributions, *e.g.* from salt-induced stresses, can also be of importance, and are briefly discussed.

1 Introduction

Methane hydrates exist in association with rock-forming minerals on the Earth and likely elsewhere in the solar system and beyond. The most common rock-forming minerals in the Earth's crust are quartz and feldspars, comprising more than 50% of the crust. Indeed quartz and feldspars are also known in other bodies, where hydrates have also been detected or hypothesized, such as Mars, various planetary moons and asteroids. Methane hydrates exist in states outside their respective ordinary temperature and pressure windows of thermodynamic stability through the formation of a stabilizing ice layer.[1–6] This observed effect is referred to as 'self-preservation' or 'anomalous stabilization'.[5,7] It has been assumed[5,7] that anomalous stabilisation occurs when a gas diffusion barrier of ice forms on the outside of the methane hydrate particles, retarding the hydrate decomposition on decompression. This ice layer has been generally thought to form kinetically as the hydrate partially depletes its outer hydrate cages close to its stability field boundary, either in water or in air. The final ice layer can give anomalous stability over short to long time scales and is an effective diffusion barrier because of the annealing of common hexagonal ice (Ih) domains to form a continuous layer, often passing through an initial cubic ice phase to a hexagonal one *via* a change in the density of stacking faults with time.[7,8] The diffusion barrier appears to be enhanced, as the stacking faults are reduced when annealing is near completion. This occurs most effectively just below 273 K, and in relatively low salinity water[9] (less than 0.5 wt% NaCl) where the freezing point depression of water is not so pronounced. The anomalous stabilization occurring for higher salinity, *i.e.*, larger than 0.5 wt% NaCl, is less effective and depressed in temperatures close to 250–260 K.

Indeed, the permafrost hydrates are hosted within porous rocks, comprising various minerals, and the effect of the stabilizing ice layers on GHs can be found when analysing onshore and offshore Arctic hydrates associated with permafrost, where some GHs, less than 200 m below the ground surface, have been

[a] *School of Physics and Materials Science, Nanchang University, Nanchang 330031, China. E-mail: leon@ncu.edu.cn*
[b] *Institute of Space Science and Technology, Nanchang University, Nanchang 330031, China*
[c] *Surface and Corrosion Science, Department of Chemistry, KTH Royal Institute of Technology, SE 100 44 Stockholm, Sweden*
[d] *Applied Mathematics Department, Research School of Physics and Engineering, The Australian National University, Acton ACT 2610, Australia*
[e] *Departamento de Física de Materiales and Instituto de Ciencia de Materiales Nicolás Cabrera, Universidad Autónoma de Madrid, 28049 Madrid, Spain*
[f] *Faculty of Science and Technology, Norwegian University of Life Sciences, Ås, Norway*
[g] *European Laboratory for Non-Linear Spectroscopy (LENS), Via Nello Carrara 1, Sesto F.no 50019, Italy*
[h] *Department of Physics and Technology, University of Bergen, Allégaten 55, 5007 Bergen, Norway*
[i] *Physikalisches Institut, Albert-Ludwigs-Universität Freiburg, Hermann-Herder-Str. 3, 79104 Freiburg, Germany*
[j] *Homer L. Dodge Department of Physics and Astronomy, University of Oklahoma, Norman, Oklahoma 73019, USA. E-mail: kmilton@ou.edu*
[k] *Department of Energy and Process Engineering, Norwegian University of Science and Technology, NO-7491 Trondheim, Norway. E-mail: iver.h.brevik@gmail.com*
[l] *Centre for Materials Science and Nanotechnology, Department of Physics, University of Oslo, P. O. Box 1048 Blindern, NO-0316 Oslo, Norway. E-mail: mathias.bostrom@smn.uio.no*
[m] *Centre of Excellence ENSEMBLE3 Sp. z o. o., Wolczynska Str. 133, 01-919, Warsaw, Poland*
[n] *Departamento de Física de la Materia Condensada, ICMSE-CSIC, Universidad de Sevilla, Apdo. 1065, 41080, Sevilla, Spain*

considered unstable.[10] However, even outside the window of stability of a specific GH,[10] dissociation is not immediate. Instead, accounting for different sinks that prevent GH methanes from reaching the atmosphere, Ruppel and Kessler suggest a timescale of 400 000 years for complete transfer.[10] Chuvilin, Shakhova and others,[11–13] have found that hydrates in permafrost regions can possibly exist at depths 0–200 m from the surface, whereas others have deemed it unlikely, and argue that the anomalous stablization of the water–ice layers is effective only under specific conditions.

We will here proceed as in a recent work,[14,15] where an energy contribution essential for the existence of relatively thick, molecular scale ice coatings on partially degassed hydrates in ice-cold water,[15] was proposed. By using reliable dielectric optical properties of water, ice, and GHs combined with a model for the Casimir–Lifshitz energy there, it was established how nano- to micron-sized ice-coated type-I CO_2 clathrates can float in water columns of ocean worlds, potentially forming thermally insulating coatings deposited on top of these oceans, underneath or within the ice caps.[15] Our past findings[15] were in line with an earlier work that modelled the observed geophysics on Pluto.[16]

In this paper, a theory of the Casimir–Lifshitz free energy, which supports the anomalous stabilization of methane GHs near a rock surface, is presented. The necessity for the formation of stabilizing ice layers is that the Lifshitz energy for a five layered system with GHs (including separate surface regions) in contact with ice and water inside the pore has an energy minimum at some specific ice layer thicknesses. Given the presence of large amounts of methane hydrates hosted in contact with rock-forming minerals in permafrost and in continental shelf sediments,[11,17] we extend our previous studies on gas hydrate stabilisation due to Casimir-force-induced ice layers to a simple model of mineral-lined rock pores interacting with methane hydrates. Also, the current work could potentially explain why GHs confined in nanopores have more stable ice layers compared to GHs in larger pores.[6] Methane hydrate is stable in small quartz cavities even outside the normal stability window (pressures and temperatures) as long as the system is below the freezing temperature of water. This experimentally observed effect is here proposed (at least partly) to be due to anomalously stabilizing ice layers formed by Casimir–Lifshitz interactions at the ice–water interface, when GHs are confined within small water-filled pores in the rocky ground (*e.g.* quartz or albite), or in clay (*e.g.* kaolinite). Finally, we outline a road map to extend the present work to include other effects (*e.g.* ion free energies).

The left panel in Fig. 1 presents a schematic illustration of our model system, which is represented as a closed pore, connected to a larger pore system out of the plane of the figure. This idealised pore is large compared to the layer thicknesses such that it is possible to model a locally flat five-layered system. We assume a cavity containing gas hydrate as the initial state, and assume some loss of methane from the surface layer of the hydrate which could be approximated as a single gas-depleted low occupancy layer. We model this system at the temperature and pressure of the quadruple point, where water and ice coexist with methane hydrate in the pore.

2 Theory

2.1 Material modelling

2.1.1 Permittivity of water and ice. The key inputs required to calculate Casimir–Lifshitz energies are the dielectric

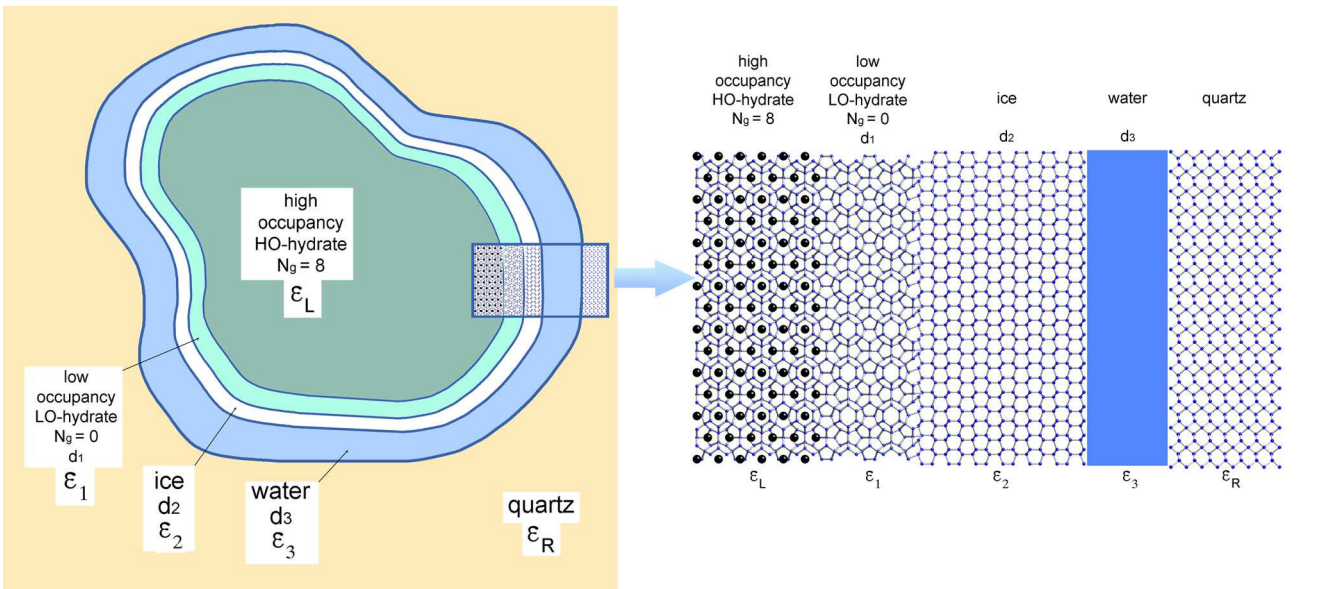

Fig. 1 Left: Schematic representation of an idealised filled pore or cavity in a rock composed of quartz. In our model, quartz and high-occupancy (HO) hydrate are infinite half spaces with respective dielectric functions ε_R and ε_L. Between these half spaces we model successive layers of low-occupancy (LO) hydrate, ice, and water. The corresponding layer thicknesses are d_1, d_2 and d_3, and the respective dielectric functions are ε_1, ε_2 and ε_3. Right: Detailed cross section of the system plotted on the left. Schematic diagram of the five-layer CH_4 hydrate system: high-occupancy (HO) gas hydrate ε_L; low-occupancy (LO) hydrate, ε_1; pure H_2O ice, ε_2; pure liquid H_2O, ε_3, and rock surface, ε_R.

functions of the interacting materials. Recently, Fiedler *et al.*[18] showed that reparameterizing the real and imaginary dielectric function of cold water results in the prediction of the formation of micron-sized ice layers at water surfaces, in contrast to the ice premelting found with the older parameterizations by Elbaum and Schick.[19,20] The result found in ref. 18 was subsequently confirmed[21] using the more recent reparameterizations of ice and water by Luengo-Márquez and MacDowell.[22,23] In the current work, we use the parameters from Luengo-Márquez and MacDowell for ice and water,[22,23] but evaluate the dielectric functions at the quadruple point of methane GH (T = 272.9 K). One should note that the parameterised models for ice and water by Luengo-Márquez and MacDowell agree well (except at very low frequencies) with the dielectric functions for imaginary frequencies derived from experimental data on the real frequency axis, but they do not obey Kramers–Kronig relation (causality) which is valid for the model by Fiedler *et al.*

2.1.2 Permittivity of quartz, albite and kaolinite. To model rock materials, quartz, albite and kaolinite are considered, whose dielectric functions were obtained with density functional theory (DFT) using the VASP software package[24–26] starting from experimental lattice constants.[27–29] Both electronic and vibrational contributions to the dielectric function at finite frequencies were taken into account. The electronic contributions were obtained within the independent-particle approximation using the HSE06 hybrid functional,[30,31] which provides more accurate band gaps than standard DFT calculations in the generalized gradient approximation (GGA). Phonon modes and Born effective charges were computed at the GGA-level of theory. The energy cutoff was set to 400 eV and the Brilloin-zone was sampled using a k-point density of 0.33 Å^{-1}. The dielectric function was carefully converged (using visual inspection) with the number of electronic bands, using respectively 200, 300, and 400 for quartz, kaolinite, and albite, reflecting the different number of atoms in the unit cells.

2.1.3 Modelling methane hydrates of different occupancy. Hydrates consist of water and gas molecules forming solid ice-like structures. Larger molecules can form type-I clathrate structures, while type-II clathrate structures typically host smaller molecules.[17] Methane hydrates pack in the type-I clathrate structures.[17] In such a system, voids can be either filled or partially degassed. The surface region could, due to diffusion, have a lower density of gas molecules than the bulk region. We model the permittivity for methane hydrates with a simple mixing model considering water and methane molecules in a frozen structure. Such a model for methane hydrate ($\varepsilon_{\mathrm{mh}}$) is described in our past works,[14,15] except here we use the improved model for dielectric function of ice,[22] ε_{i}, in the Lorentz–Lorenz model[32] within the mixing scheme for GHs taken from Bonnefoy *et al.*[33,34]

$$\varepsilon_{\mathrm{mh}}(i\zeta; N_{\mathrm{g}}) = \frac{1+2\Gamma}{1-\Gamma}, \tag{1}$$

with

$$\Gamma = \frac{\varepsilon_{\mathrm{i}}-1}{\varepsilon_{\mathrm{i}}+2}\frac{n_{\mathrm{wh}}}{n_{\mathrm{i}}} + \frac{4\pi\alpha_{\mathrm{M}}n_{\mathrm{M}}}{3}, \tag{2}$$

where n_{i} is the number density of water molecules in ice, while n_{wh} and n_{M} are the number densities of water and gas molecules in the hydrate structure, respectively, and α_{M} is the gas polarizability. Eqn (2) means that the dominating factors for the dielectric function of GHs are the ice polarizability $(\varepsilon_{\mathrm{i}}-1)/(\varepsilon_{\mathrm{i}}+2)$ weighted by the number density of water in the hydrate relative to pure ice, and the polarizabilities of different gas molecules weighted by their corresponding number densities. The mass density of water in pure ice[35] is 0.9167 g cm^{-3}, giving the number density of water molecules in pure ice as n_{i} = 3.06434 × 10^{-2} Å^{-3}. The number densities of water molecules (n_{wh} = 2.65681 × 10^{-2} Å^{-3}) and gas molecules ($n_{\mathrm{M}} = N_{\mathrm{g}} \times n_{\mathrm{wh}}/46$) in methane GH structures were all derived following the work by Prieto-Ballesteros *et al.*[36] (and references therein). The number N_{g} of gas molecules per 46 water molecules in the GH unit cell can vary with occupancy: N_{g} = 0 (empty), 1, 2, 3,..., 8 (fully occupied).[36] Later on in this work, for example in Section 3.1.2, a distinction is made between surface (s) and bulk (b) regions, replacing N_{g} with the more specific $N_{\mathrm{g,s}}$ and $N_{\mathrm{g,b}}$ values, respectively. Calculations to obtain quantum chemical dynamic polarisabilities at discrete frequencies were fitted at arbitrary imaginary frequencies $i\xi$ to the 5-mode oscillator model,[14]

$$\alpha_{\mathrm{M}}(i\zeta) = \sum_j \frac{\alpha_j}{1+(\zeta/\omega_j)^2}. \tag{3}$$

The adjusted parameters for CH_4 were given in our recent work.[37] This describes the dynamic polarisability accurately up to a very small (0.02%) relative error.[38]

2.1.4 Overview of different materials' permittivities. The dielectric functions we model above are valid for materials at temperature T = 273.16 K. However, due to the weak dependence of dielectric functions on pressure and the proximity to the quadruple point temperature of CH_4 gas hydrates, we can use, to a good approximation,[14] the same parameterised dielectric functions at the quadruple point for methane hydrate (p = 25.63 bar and T = 272.9 K).[17] Fig. 2 shows the dielectric functions (at T = 272.9 K) employed in this work for water[22,23] and ice,[22,23] together with those for quartz, albite, kaolinite, and methane hydrate with different gas molecular occupancies. We observe that the curve for ice (in cyan) lies above the low occupancy GH curves, and below the high occupancy curves, which will result in different effects on ice formation depending on the occupancy. In contrast, the curve for water (in green) is above the curves of all considered GHs (thus, above the ice curve) indicating that the Casimir–Lifshitz interaction alone cannot lead to premelting of ice in contact with a methane hydrate surface. The three curves on the top (for quartz, albite and kaolinite) in Fig. 2 are very close to each other, and the relative magnitudes of these three permittivities with respect to different materials at zero frequency only yield tiny qualitative differences in the Casimir–Lifshitz interaction, as will be shown in Fig. 10. For these reasons, we focus our studies just on quartz in combination with ice, water and different methane hydrates to address the study of Casimir–Lifshitz interactions. We also study the effects on the Casimir–Lifshitz interaction from using different rock materials, by comparing the corresponding

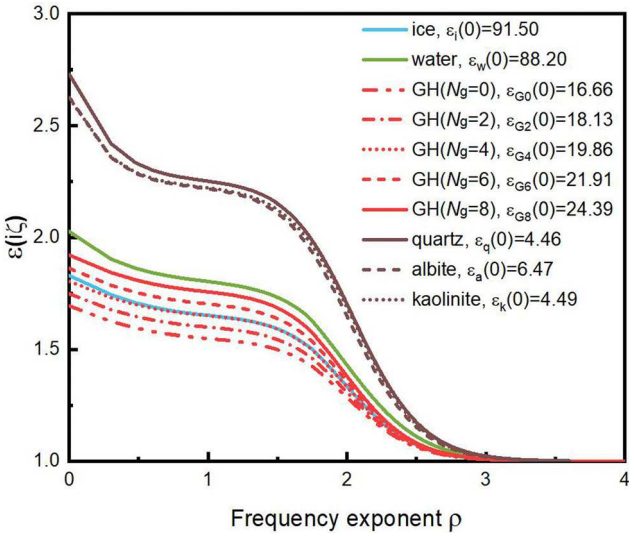

Fig. 2 Dielectric functions for fully occupied (N_g = 8) methane GH, low occupancy (N_g = 0, 2, 4, 6) methane GH, pure H_2O ice, pure liquid H_2O, quartz, albite, and kaolinite, as functions of the exponent ρ, in which ρ is defined as $\rho = \log_{10}\zeta/\zeta_T$ with $\zeta_T = 2\pi T$ being the first nonzero Matsubara frequency at the temperature of the quadruple point of methane GHs, 272.9 K. The static values of the dielectric constants for each material ε_X are given in the legend.

stresses induced. Indeed, when exploiting the similar dielectric functions found from DFT for quartz, albite and kaolinite, we find only small variations for the Casimir–Lifshitz forces and stresses, as it will be shown in Fig. 10. Other sets of materials, material models, or type of interactions (*e.g.* salt induced pressures), may lead to predictions with a larger diversity. In addition, based on the relative differences amongst the permittivities of the different materials considered in Fig. 2, we can qualitatively estimate the configurations in which the ice coating could be stabilized by Casimir–Lifshitz interactions, as was done for other material combinations.[21] In what follows, we will analyze anomalously stabilized ice layers in cavities modelled within a five layer Casimir–Lifshitz theory. The derivation of this theory is given in the Appendix, and discussion on ionic interactions and other non-Lifshitz effects are provided in Section 4.2.

2.2 Casimir–Lifshitz interaction in multi-layer inhomogeneous systems

Lifshitz and co-workers derived the dispersion force between interacting planar media.[39] Afterwards, Ninham and co-workers simplified the theoretical modelling of Casimir–Lifshitz dispersion forces in the early 1970s.[40–43] The original Lifshitz theory applied to just one intermediate layer (between the interacting materials) which, for sufficiently large thicknesses, could be taken as semi-infinite. Recently, it was demonstrated, in the case of a four-layer geometry,[22,44] how to extend the theory to two intervening layers, which separately, might take infinite thickness. The extension to consider multi-layer magnetodielectric induced stress is straightforward and it arises from the difference in magnetodielectric Casimir–Lifshitz forces[22,44–49] in two adjacent media. Here, we consider four- and five-layer configurations, with ice and water as the two intervening layers. To evaluate the Casimir–Lifshitz interactions in these configurations, the intervening media are treated as inhomogeneous and the theoretical framework proposed in ref. 48 is employed. With the inhomogeneous description, the Casimir–Lifshitz interaction in a general n-slab structure can be obtained and is consistent with present results, as detailed in the Appendix.

2.2.1 Four-layer configuration. For the four-layer configuration,[44] the stress across the ice–water interface induced by Casimir–Lifshitz interactions, *i.e.* across layer 2 and 3 following the scheme in Fig. 1 (right panel), takes into account the pressure contributions from both sides, that is,

$$P_{\mathrm{CL};23} = P_{\mathrm{ice,right}} + P_{\mathrm{water,left}}. \tag{4}$$

As $P_{\mathrm{water,left}} = -P_{\mathrm{water,right}}$, we have

$$P_{\mathrm{CL};23} = P_{\mathrm{ice,right}} - P_{\mathrm{water,right}}. \tag{5}$$

Suppose these four layers are stacked horizontally along the positive z-direction from medium 1 to medium 4 without losing any generality. A positive stress thus corresponds to a force directed rightwards, in the direction of positive z. In simple terms, outward pointing pressures on the ice layer and on the water layer have opposite directions at the ice–water interface. The surface stress on the ice–water interface due to the Casimir–Lifshitz interaction, acting from the ice side, is then†

$$P_{\mathrm{CL};23} = -\frac{T}{2\pi}\sum_{m=-\infty}^{\infty}\int_0^{\infty} dkk \sum_{s=\mathrm{E,H}}\left(\frac{\kappa_2}{D_2^s} - \frac{\kappa_3}{D_3^s}\right), \tag{6}$$

in which the sum is over Matsubara frequencies $\zeta_m = 2\pi T|m|$, with $m \in \mathbb{Z}$, and E, H represent transverse electric (TE) and transverse magnetic (TM) polarizations (also commonly denoted by s and p), respectively. The multiple reflections between the interfaces, as described by Esteso *et al.*[44] give the mode structures

$$\frac{1}{D_2^s} = \frac{-r_{12}^s \bar{r}_{23}^s \mathrm{e}^{-2\kappa_2 d_2}}{1 + r_{12}^s \bar{r}_{23}^s \mathrm{e}^{-2\kappa_2 d_2}}, \quad \frac{1}{D_3^s} = \frac{-r_{43}^s \bar{r}_{32}^s \mathrm{e}^{-2\kappa_3 d_3}}{1 + r_{43}^s \bar{r}_{32}^s \mathrm{e}^{-2\kappa_3 d_3}}, \tag{7}$$

where d_2, d_3 are the thicknesses of layer 2 and 3, respectively. Here we use the imaginary part of perpendicular wavevector[43]

$$\kappa_n = \sqrt{k^2 + \mu_n(i\zeta_m)\varepsilon_n(i\zeta_m)\zeta_m^2}, \tag{8}$$

where $k = |\mathbf{k}|$ is the magnitude of the wavevector parallel to the surface. For nonmagnetic materials, the permeability satisfies $\mu(i\zeta_m) = 1$ for all m values. The reflection coefficients at a single interface, r_{ij}^s, are given as eqn (28) in the Appendix, along with the reflections at multiple interfaces,[45,46,50] $\bar{r}_{ij}^s$, in eqn (36) for the four-layer geometry.

2.2.2 Five-layer configuration. For the five-layer case, the pressure on a surface, for instance the surface between medium 2 and 3, has the same form as in eqn (6), except that D_2^s and D_3^s

† We utilize the natural units $\hbar = \varepsilon_0 = \mu_0 = c = k_B = 1$ throughout, unless specified.

take the form

$$D_2^s = \frac{e^{2\kappa_2 d_2}}{\bar{r}_{23}^s \bar{r}_{21}^s} - 1,\ D_3^s = \frac{e^{2\kappa_3 d_3}}{r_{3R}^s \bar{r}_{32}^s} - 1. \quad (9)$$

Here the reflection coefficients at multiple interfaces are given in the Appendix in eqn (50a–c). The corresponding Casimir–Lifshitz free energy in this inhomogeneous five-layer structure is given by

$$F_{CL} = \frac{T}{2} \sum_{m=-\infty}^{\infty} \int \frac{d^2k}{(2\pi)^2} \ln \Delta^E \Delta^H, \quad (10)$$

with Δ^E given from eqn (46) in the Appendix, and Δ^H obtained by making the substitution $\varepsilon \leftrightarrow \mu$ in the same expression. As mentioned above, detailed derivations for the Casimir–Lifshitz stress and free energy in general n-layered inhomogeneous media are given in the Appendix. We bring here the specific expression of F_{CL} in a five-layer system [eqn (46) in Appendix.]

$$\begin{aligned} F_{CL} = T \sum_{m=0}^{\infty}{}' \int \frac{d^2k}{(2\pi)^2} \sum_{s=E,H} \ln \Big[& 1 + r_{L1}^s r_{12}^s e^{-2\kappa_1 d_1} + r_{12}^s r_{23}^s e^{-2\kappa_2 d_2} \\ & + r_{23}^s r_{3R}^s e^{-2\kappa_3 d_3} + r_{L1}^s r_{23}^s e^{-2(\kappa_1 d_1 + \kappa_2 d_2)} + r_{12}^s r_{3R}^s e^{-2(\kappa_2 d_2 + \kappa_3 d_3)} \\ & + r_{L1}^s r_{3R}^s e^{-2(\kappa_1 d_1 + \kappa_2 d_2 + \kappa_3 d_3)} + r_{L1}^s r_{12}^s r_{23}^s r_{3R}^s e^{-2(\kappa_1 d_1 + \kappa_3 d_3)} \Big], \end{aligned} \quad (11)$$

in which the primed sum means the $m = 0$ term is counted in its half weight. A high symmetry is seen in the expression for F_{CL}, and its consistency with four-layered and three-layered configurations are obvious. Note, however, that the thickness of one or two of the layers going to zero involves subtleties, as described in detail in the Appendix.

2.2.3 Non-retarded limits. Thicknesses of intervening materials involved when considering premelting and formation of ice are typically on the nano- to micro-scale.[14,15,18–21] Around the quadruple point of methane hydrate (at T = 272.9 K), the wavelength corresponding to the m = 1 Matsubara frequency is $\lambda_T \approx 1.36$ μm. This means that in systems with relatively thin mediating layers (several or few tens of nanometers), non-retarded interaction will be sufficient to outline the main properties of the Casimir–Lifshitz interaction. However, when the thickness of the mediating layers becomes comparable with 1 μm, the retardation effect would inevitably and significantly modify the non-retarded contributions. On the one hand, retardation effects are usually thought to not alter the repulsive or attractive character of the contribution to the Casimir–Lifshitz stress from each Matsubara term, which could facilitate qualitative estimations. On the other hand, these repulsive and attractive effects are vital for the premelting and formation phenomena investigated here. It is thus worthwhile, in this work, to give some thought to the non-retarded behaviors of multi-layer configurations, including as well three-layer structures.[51]

Firstly, we consider the simple case of a three-layer system consisting of nonmagnetic media and arranged as ε_1–ε_2–ε_3, in the non-retarded limit, where the frequency and spatial dependence separates due to the small thickness of the intervening layer d, $d \ll \zeta_1^{-1}$. In this case, the Casimir–Lifshitz free energy F_{CL} can be expressed in terms of the Hamaker constant[52,53] ($A_{123} = -12\pi d^2 F_{CL}$),

$$A_{123} = \frac{-3T}{2} \sum_{n=0}^{\infty}{}' \int_0^{\infty} dx x \ln \hat{\Delta}_{123}(\zeta_n; x), \quad (12)$$

where the coefficient $\hat{\Delta}_{123}(\zeta; x)$ is defined as $\hat{\Delta}_{123}(\zeta; x) = 1 + \hat{r}_{12}(\zeta)\hat{r}_{23}(\zeta)e^{-x}$, the reduced reflection coefficient $\hat{r}_{ij}$ is

$$\hat{r}_{ij}(\zeta) = \frac{\varepsilon_j(i\zeta) - \varepsilon_i(i\zeta)}{\varepsilon_j(i\zeta) + \varepsilon_i(i\zeta)}, \quad (13)$$

and the corresponding zero frequency Hamaker constant ($A_{123;0}$) takes the form

$$A_{123;0} = \frac{-3T}{4} \int_0^{\infty} dx x \ln \hat{\Delta}_{123}(0; x). \quad (14)$$

As previously pointed out,[54] the m = 0 frequency Matsubara term sometimes has the opposite sign to the rest of finite frequency terms. For the case here, a positive sign for A_{123} (or $A_{123;0}$) indicates short range (or long range for $A_{123;0}$) attraction, while a negative sign indicates repulsion.[51] The different separation regimes for the three-layer interaction are short range non-retarded regime (free energy $\propto d^{-2}$), retarded regime (free energy $\propto d^{-3}$), and the long-range thermal regime (free energy $\propto d^{-2}$). Here, the retardation leads to a reduction of the $m > 0$ contributions to the Casimir–Lifshitz free energy, leaving long-range results dominated by the m = 0 term (as long as the effect of screening from ions on the m = 0 term at very large separations is negligible). Hence, for a water–ice–vapor system, the relation of the dielectric function fulfils $\varepsilon_1 > \varepsilon_2 > \varepsilon_3$ for finite frequencies, while the relation $\varepsilon_2 > \varepsilon_1 > \varepsilon_3$ is attained at zero frequency. We thus find a negative A_{123} (repulsion) and a positive $A_{123;0}$ (attraction) zero frequency Hamaker constant, indicating that the formation of a finite size ice layer on a water surface at the triple point of water is possible, as it was recently predicted based on the complete Casimir–Lifshitz theory using a revised and improved set of dielectric functions.[37] The argument relating relative magnitudes of dielectric functions in a three layer structure to either attraction or repulsion, which can be understood by considering eqn (12) and (14), goes back to the original work by Dzyaloshinskii, Lifshitz, and Pitaevskii (DLP).[39] As an illustration, the different three-layer Hamaker constants relevant for us are given in Table 1. For three-layer configurations, the intervening layer would be stabilized by a repulsive short-range and attractive long-range Casimir–Lifshitz force. So only specific GH–ice–water and GH–ice–quartz configurations with low enough occupancy numbers for GH, and GH–water–quartz satisfiy this criterion. Particularly, for the GH–ice–water–quartz structure, the consequences of the competition between the formation of ice in the short range, due to GH–ice–water, and the expansion of the water phase due to the ice–water–quartz data in Table 1, are not obvious and therefore require explicit evaluations as done in Section 3.

Table 1 The Hamaker constant A_{123} and its contributions from the zeroth Matsubara term $A_{123;0}$ for various three-layer configurations

Configurations (1–2–3)	N_g	A_{123} (meV)	$A_{123;0}$ (meV)
GH–ice–water	0	-6.00×10^{0}	2.25×10^{-1}
	4	-3.48×10^{-2}	2.09×10^{-1}
	8	5.89×10^{0}	1.88×10^{-2}
GH–water–ice	0	1.87×10^{1}	-2.21×10^{-1}
	4	1.27×10^{1}	-2.05×10^{-1}
	8	6.82×10^{0}	-1.83×10^{-1}
GH–ice–quartz	0	-8.53×10^{0}	1.22×10^{1}
	4	1.04×10^{1}	1.12×10^{1}
	8	2.90×10^{1}	1.00×10^{1}
GH–water–quartz	0	-3.03×10^{1}	1.20×10^{1}
	4	-1.73×10^{1}	1.10×10^{1}
	8	-4.65×10^{0}	9.72×10^{0}
Ice–water–quartz	—	-2.80×10^{1}	-2.92×10^{-1}
Ice–water–albite	—	-2.25×10^{1}	-2.79×10^{-1}
Ice–water–kaolinite	—	-2.57×10^{1}	-2.92×10^{-1}
Water–ice–vapor	—	-4.74×10^{1}	3.18×10^{-1}
Ice–water–vapor	—	5.98×10^{1}	-3.16×10^{-1}

Also these arguments provide a useful framework leading to some intuitive understanding in the more complicated multi-layer cases considered in this work, mainly four- and five-layer configurations. As already known, in a four-layer system, the contribution from four-layer interactions to the Casimir–Lifshitz free energy can be derived as $F_{14} = F_{CL} - F_{123} - F_{234}$, in which F_{123}, as well as F_{234}, is the Casimir–Lifshitz free energy of the three-layer (or DLP) configuration. When thicknesses of the intervening layers (2 and 3) are very small, the non-retarded limit leads us to the Hamaker constant for F_{14} as

$$A_{14} = \frac{-3T}{2}\sum_{n=0}^{\infty}{}' \int_0^{\infty} \mathrm{d}x x \ln\left[1 + \frac{\hat{r}_{12}(1-\hat{r}_{23}^{2})\hat{r}_{34}\mathrm{e}^{-x}}{\hat{\Delta}_{123}(\zeta_n; x\eta_2)\hat{\Delta}_{234}(\zeta_n; x\eta_3)}\right], \tag{15}$$

in which $\eta_i = d_i/d$ and $d = d_2 + d_3$ is the total thickness of intervening layers. In the non-retarded limit, the Casimir–Lifshitz free energy in this four-layer system is

$$F_{CL}^{(nr)} = \frac{-A_{1234}}{12\pi d^2},\ A_{1234} = \frac{A_{123}}{\eta_2^{2}} + \frac{A_{234}}{\eta_3^{2}} + A_{14}. \tag{16}$$

Similar generalizations apply to five-layer configurations, giving the relations satisfied by the five-layer interaction Hamaker constants A_{15} and the total one A_{1-5} as follows

$$A_{1-5} = \frac{A_{1234}}{(1-\eta_4)^2} + \frac{A_{2345}}{(1-\eta_2)^2} - \frac{A_{234}}{\eta_3^{2}} + A_{15}, \tag{17}$$

where now $d = d_2 + d_3 + d_4$. For inhomogeneous multi-layer configurations, the details of mediating layers introduce extra complexities as we shall see below.

3 Results

3.1 Predictions based on Casimir–Lifshitz free energy considerations

3.1.1 Uniformly filled GH. Suppose a uniform methane GH material filling a cavity is covered by two intervening layers, namely ice and water layers, near a rock surface. Since the distance between the outer surface of methane GH and the wall of the rock cavity is almost fixed, it is reasonable to treat the total thickness d of these ice and water layers as a constant. Consider, first, a representative case with a total thickness of the intervening layers being d = 1 μm. Fig. 3 shows that the anomalously stabilizing ice layer on the GH tends to be suppressed by the Casimir–Lifshitz interaction when it has a relatively high occupancy ($N_g \geq 6$). When the occupancy number decreases, a clear-cut minimum of free energy occurs, for instance an ice layer of about 3 nm with N_g = 4. For lower occupancies, a relatively wide range of anomalously stabilizing ice layer thicknesses, of about 100–700 nm, are allowed to form. However, relatively minor perturbations can modify the ice thickness formation, and hence, alter the ability to prevent leakage of gas molecules. Yet, for very thin ice layers, a strong repulsive Casimir–Lifshitz stress acts against further melting. Notably, it would appear that, for a uniform bulk GH, the more gases stored in it, the less stable its ice layer will be.

Furthermore, the fixed total thickness of ice and water layers, or the size of GH compared to the volume of cavity, is also important to the stability of the self-preserving ice film. Fig. 4 shows a specific case examined in Fig. 3 corresponding to the methane GH–ice–water–quartz configuration with the occupancy number of GH being N_g = 0. As the distance between the GH and the cavity wall, d, decreases, the ice layer tends to become thinner. However, it is evident that when d decreases, the Casimir–Lifshitz interaction gains a stronger ability to stabilize a nano- to micron-sized ice layer on this GH (for the d = 500 nm case here, its thickness is about 170 nm).

To illustrate the influence of the presence of quartz rock, we evaluate the relevant three-layer scenarios in Fig. 5. The effect of this presence, as shown in Fig. 4, is significant only when the thickness of intervening layers is not large. The formation of ice

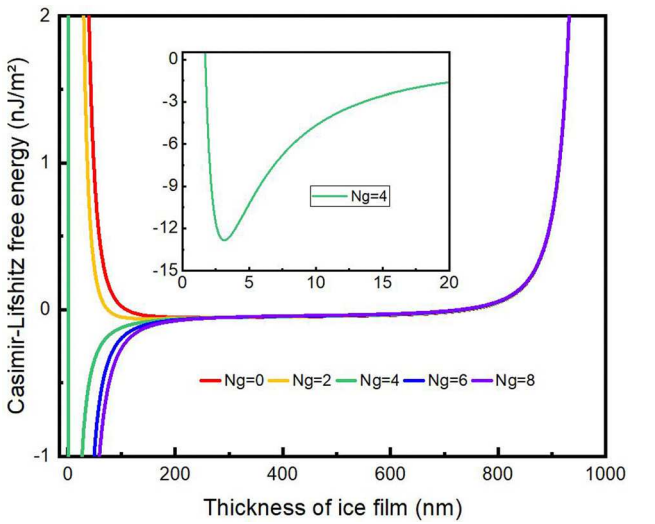

Fig. 3 The Casimir–Lifshitz free energy per unit area in four-layer systems, namely the methane GH (GH)–ice–water–quartz, varying with the thickness of medium 2, which is ice here, while the total thickness of ice and water layers, denoted as d, is fixed to d = 1000 nm. The influence of different occupancy number N_g of cages in the GH is also shown.

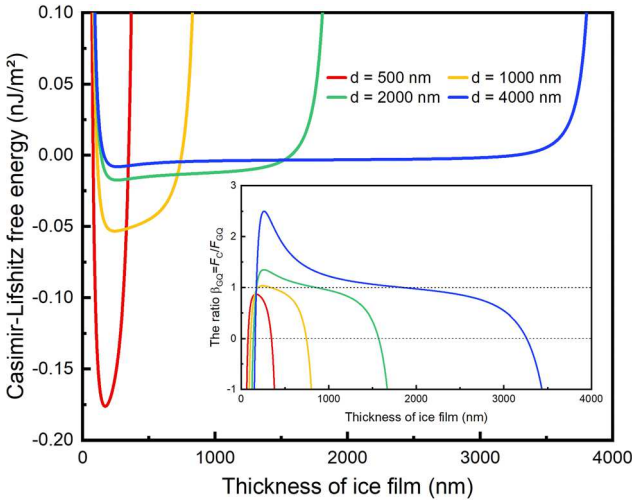

Fig. 4 The Casimir–Lifshitz free energy per unit area in the methane GH (N_g = 0)–ice–water–quartz, varying with the thickness of ice film for different fixed total thickness d of ice and water layers. The inset shows the ratio $\beta_{GQ} = F_{CL}/F_{GQ}$, where F_{GQ} is the four-layer contribution obtained by subtracting the GH–ice–water and ice–water–quartz contributions from the total Casimir–Lifshitz free energy F_{CL}, for the same settings corresponding to the same color lines.

layer for four-layer cases as those in Fig. 3 and 4 behaves similarly to the GH in a bulk of water without any other restrictions, when the total thickness of the intervening ice and water layers is sufficiently large. This can be deduced by comparing Fig. 3 and the bottom panel in Fig. 5. The shallow energy minimum for an empty GH structure in contact with cold water occurs at an ice layer thickness of about 265 nm (to guide the eye, it is marked with a vertical dashed line in the bottom panel of Fig. 5). On the other hand, for the methane GH–ice–quartz structure, an ice layer forms only when the GH has a very small occupancy number, and the intermediate layer

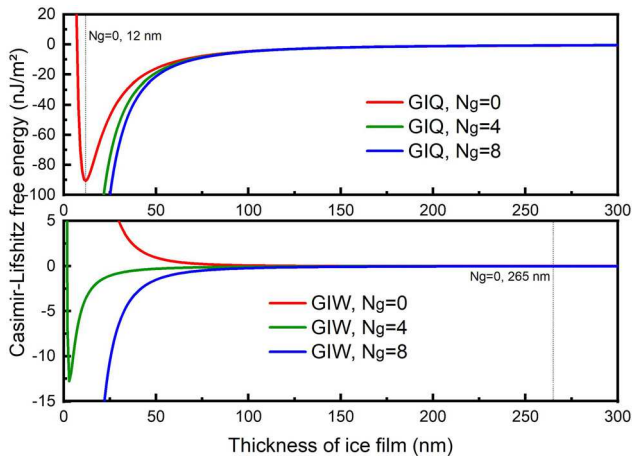

Fig. 5 The Casimir–Lifshitz free energy per unit area in three-layer configurations: methane GH–ice–quartz (GIQ) (top panel), and methane GH–ice–water (GIW) (bottom panel), varying with the thickness of ice film, for different occupancy number N_g of cages in the GH. The labels denote positions of the minima of the free energy.

is thin (about 12 nm for N_g = 0 case, as in the top panel in Fig. 5). So, in general, for the relatively large separation distance between the GH and the micron-sized quartz material, a single ice layer cannot fill in the whole space as an intervening layer typically.

3.1.2 GH with specific surface layers. As shown above, for the pure GH in a cavity, a naive guess is that its capability to store the methane gas is quite limited because, as the number of gas molecules increases, the Casimir–Lifshitz interaction tends to prevent the formation of the anomalously stabilized ice layers. Practically, however, the concentration or dilution could happen near the surface of the GH, which complicates the interaction and the related phenomena. It was recently predicted[15] that nano- to micron-sized anomalously stabilized ice layers can form *via* Casimir–Lifshitz interactions on GHs, with a low-occupancy surface region in contact with cold water. Note that while a depleted surface region is physically realistic, a GH with a bulk region totally depleted of gas molecules is thermodynamically unstable. In the following section we will demonstrate that a proper understanding of the effect from confinement on anomalous stabilization requires a five-layer Casimir–Lifshitz model. It enables us to include separate bulk and surface regions for the methane GH as well as a layered structure of ice, water and rock.

Suppose the methane GH is originally fully-occupied with the occupancy number $N_{g,b}$ = 8 (the subscript b denotes that it is for bulk region), then the leakage of gas molecules, *via* thermal diffusion, might result in a thin surface region with a lower occupancy number $N_{g,s} < 8$ (the s here stands for the surface region). When the surface of GH is not so empty, for instance $N_{g,s}$ = 6, the ice coating is still suppressed. But when $N_{g,s}$ = 4, this thin surface of GH facilitates the growth of ice. However, its capability is quite limited, and an ice film at most about 3 nm thickness appears when the surface GH is thick enough. For the surface with a lower occupancy number, the increasing surface thickness leads to an increasing equilibrium ice film thickness. As shown in Fig. 6, for $N_{g,s}$ = 0 and $N_{g,s}$ = 2 cases, the respective equilibrium ice film thicknesses approach their corresponding four-layer results in Fig. 3. Therefore, by eliminating some gases stored in the surface of bulk GH, the fully-occupied bulk can be stabilized under an ice coating of a few hundreds of nanometers.

Besides the thickness of surface GH, the constraints due to the quartz cavity are also important. As shown in Fig. 7, where the $N_{g,s}$ = 0 and $N_{g,s}$ = 2 cases are given without losing any generality, when the GH is closer to the quartz cavity wall, the equilibrium thickness of ice layer will correspondingly decrease. However, when the distance between the GH and the quartz are large enough, only the thickness of surface GH determines the size of the ice layer, as can be seen from Fig. 6.

3.2 Insights from Casimir–Lifshitz stresses

3.2.1 Relation between stress and free energy results. The Casimir–Lifshitz stress approach can provide similar information as the Casimir–Lifshitz free energy approach for all the inhomogeneous scenarios considered here. This is in contrast

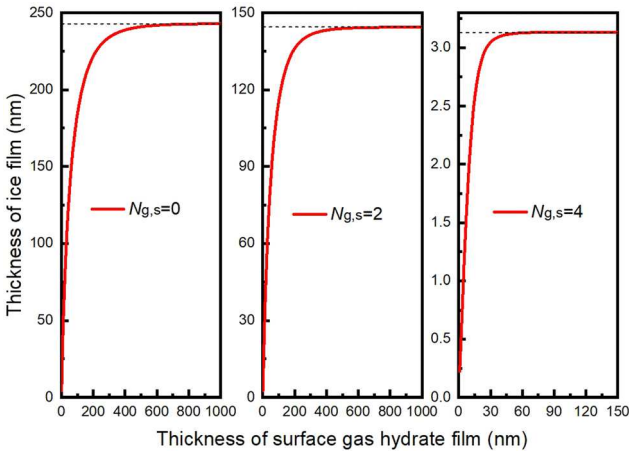

Fig. 6 The equilibrium thickness of ice layers, with the given total thickness of ice and water layers as $d = d_2 + d_3 = 1000$ nm, varying as functions of the thickness of surface GH layer in the configuration high occupied GH (bulk)-lower occupied GH (surface)-ice–water–quartz. Here as illustration we consider $N_{g,b} = 8$ and the values for $N_{g,s}$ are given in the figure.

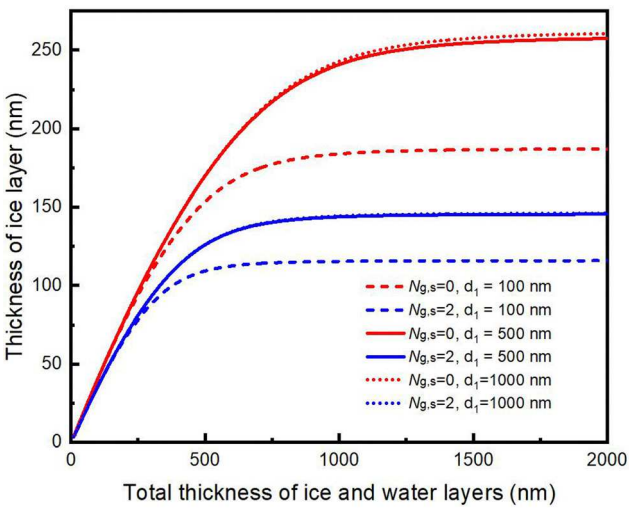

Fig. 7 The equilibrium thicknesses of ice layers, with different given thicknesses d_1 of surface GH layers, varying as functions of the total thickness of ice and water layers in the configuration high occupied GH (bulk)-lower occupied GH (surface)-ice–water–quartz. Here we consider $N_{g,b} = 8$ and the values for $N_{g,s}$ are given in the figure.

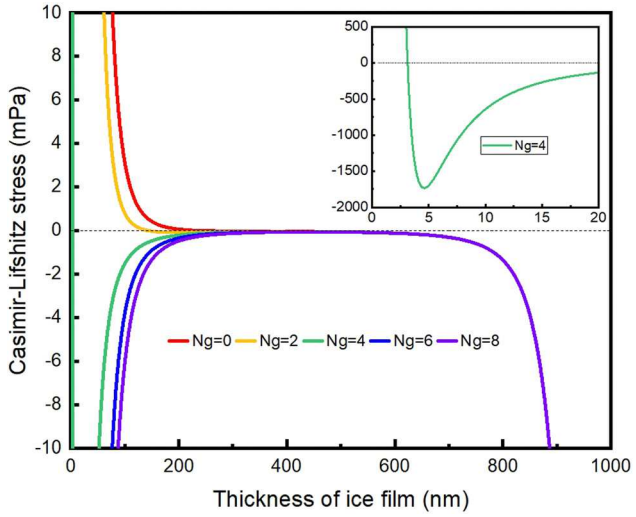

Fig. 8 The Casimir–Lifshitz ice–water stress in four-layer systems, namely the methane GH (GH)–ice–water–quartz, varying with the thickness of medium 2, which is ice here, while the total thickness of ice and water layers, denoted as d, is fixed to $d = 1000$ nm. The influence of different occupancy number N_g of cages in the GH is also shown.

to the more complicated configurations, where GH–ice–water is in contact with a flexible water vapor region. In such cases, the free energy approach is superior since positions and depths of both local and global energy minima can be predicted. Our main results in this paper come from the free energy approach, but here we also show in Fig. 8 the Casimir–Lifshitz stress of four-layer systems studied in Fig. 3. The ice–water equilibrium can be found from the thicknesses that give zero stress across the ice–water interface. According to Fig. 8, with a relatively large occupancy number, such as $N_g = 6,8$ here, the stress at the ice–water interface is always negative, implying the suppression of ice growth. When the methane GH has a lower occupancy number, for instance $N_g = 0, 2, 4$, this stress varies from positive to negative, as the thickness of the ice layer increases. Thus the repulsive Casimir–Lifshitz stress for short range promotes the ice growth, while its attractive counterpart for long range prevents further freezing, resulting in a nano- or micron-sized ice layer. These results based on Casimir–Lifshitz stress arguments are consistent with those in Fig. 3 and 6, which are also justified by comparing insets of Fig. 6 and 8. As for the five-layer configurations investigated in Fig. 6 and 7, we demonstrate in Fig. 9 the dependence of Casimir–Lifshitz stress across the ice–water interface P_{iw} and the corresponding free energy per unit area, F_{CL}, on ice and water layer thicknesses, denoted as d_2 and d_3 respectively. Their consistency with the results shown in Fig. 6 and 7 is clearly seen, which again illustrates the equivalence between stress and free energy arguments.

3.2.2 Effect on stress using three different cavity materials. As shown in Fig. 2, the dielectric functions of the examined rock (quartz and albite) and clay (kaolinite) materials are similar, especially when compared with the dielectric functions of the other materials involved in the cavities here considered, that is, ice, water, and methane GHs. Fig. 10 shows the Casimir–Lifshitz stress for three different cavities represented by a four-layer system in which the rocky material is albite (blue line, box), kaolinite (green line, triangle) or quartz (red line, circle) and $N_g = 0$. We fix the size of the cavity between the GH and the rock, and the total thickness of ice and water layers is kept constant ($d = 1000$ nm), allowing the thickness of ice to vary. Specifically, the four-layer systems considered here comprise either GH–ice–water-rock or GH–ice–water-clay. The difference between the stress and induced effects on stabilization is very small in these cases, giving rise to anomalously stabilized ice layer thicknesses of 245, 244 and 244 nm for

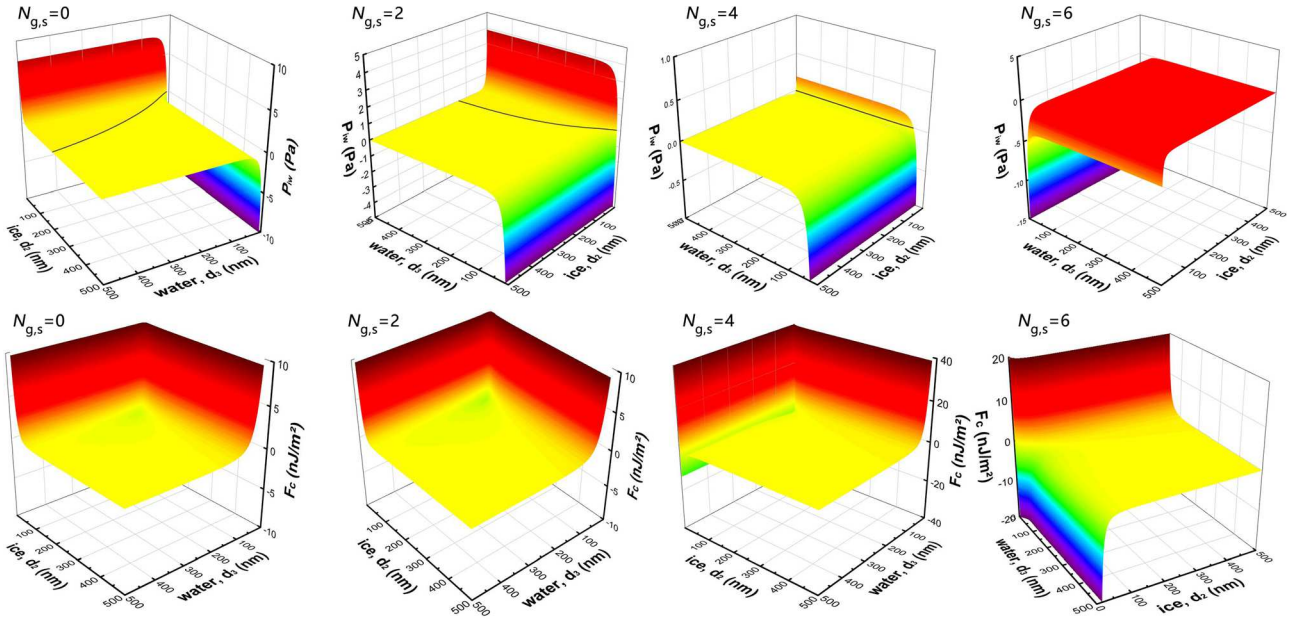

Fig. 9 Contour plots of the Casimir–Lifshitz stress across ice–water interface P_{iw} and its corresponding free energy per unit area F_{CL} as functions of ice and water layer thicknesses, denoted as d_2 and d_3 respectively, for a configuration with GH (bulk)-GH (surface)-ice–water–quartz (G_bG_sIWQ) schematically shown in right panel of Fig. 1, with various occupancy numbers ($N_{g,s}$ = 0, 2, 4, 6) of a "thick" (500 nm) layer of surface GH. The solid black curves indicate the equilibrium systems with zero stress.

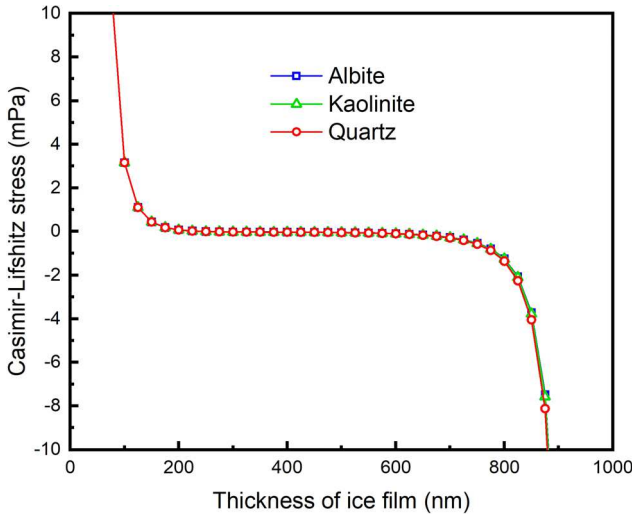

Fig. 10 The Casimir-Lifshitz ice-water stress in four-layer systems, namely the methane GH (GH)–ice–water-rock, varying with the thickness of medium 2, which is ice here, while the total thickness of ice and water layers, denoted as d, is fixed to d = 1000 nm and N_g is equal 0.

cavities formed by albite, kaolinite and quartz, respectively. Also for higher N_g values we find similar anomalously stabilized ice thicknesses. Considering N_g = 2, the stabilized ice thickness becomes 145 nm for albite and kaolinite, and 144 nm for quartz cavities, whereas when the gas molecules is set to be N_g = 4, the ice thickness is 3 nm for the three materials. However, one can imagine situations where the experimental dielectric function of specific rock or clay materials may have much stronger effects on the melting of stabilized ice layers, which merits further investigations on such effects and various geophysical applications.

4 Discussion

4.1 Analysis of the results

4.1.1 Limitations of the Hamaker approach. According to the results above, when one of the intervening layers is not thick, the interaction between its two interfaces dwarfs others. Multi-layer interactions, such as four- and five-layer interactions here, introduce more complexities compared with the three-layer cases. As detailed in the Appendix, we can extract the contribution from the pure four-layer interaction to the total Casimir–Lifshitz free energy F_{CL}, denoted as F_{GQ} for the configurations depicted in Fig. 3 and 4, by subtracting two three-layer interaction contributions, namely GH–ice–water (F_{GIW}) and ice–water–quartz (F_{IWQ}), that is, $F_{GQ} = F - F_{GIW} - F_{IWQ}$. The inset of Fig. 4 shows significances of F_{GQ}. When either ice or water layer is thin, then the interaction between the two closest interfaces of this medium dominates; while both ice and water layers are relatively thick, the four-layer interaction could contribute much more than the three-layer interactions. On the other hand, in the non-retarded limit, the contributions from the four-layer interaction are typically quite small. For example, when N_g = 0, A_{GQ} resulting from the four-layer interaction, is only about 2% of the the total Hamaker constant A at best, as illustrated by the left case of Fig. 11. This is quite different from the inset of Fig. 4 and the right cese of Fig. 11, in which we clearly see a region where $|\beta_{GQ}| < 1$, proving the influence of retardation effects.

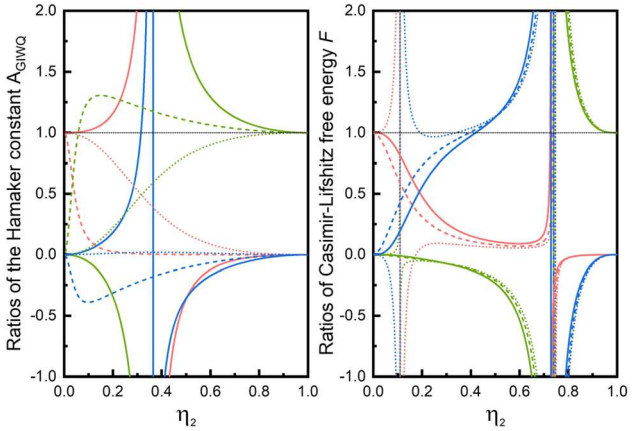

Fig. 11 Left: The ratios of the Hamaker constant $A = A_{GIWQ} = \eta_2^{-2}A_{GIW} + \eta_3^{-2}A_{IWQ} + A_{GQ}$ for the methane GH–ice–water–quartz (GIWQ) configuration relative to its contributions, namely $(\eta_2^{-2}A_{GIW})/A$ (red), $(\eta_3^{-2}A_{IWQ})/A$ (green) and A_{GQ}/A (blue), with the GHs of different occupancy numbers, N_g = 0 (dotted), N_g = 4 (dashed) and N_g = 8 (solid). Right: The corresponding Casimir–Lifshitz free energy ratios, namely F_{GIW}/F, F_{IWQ}/F and F_{GQ}/F, with the same settings as the left case and the total thickness of ice and water layers is 1000 nm. Singularities occur when A or F = 0.

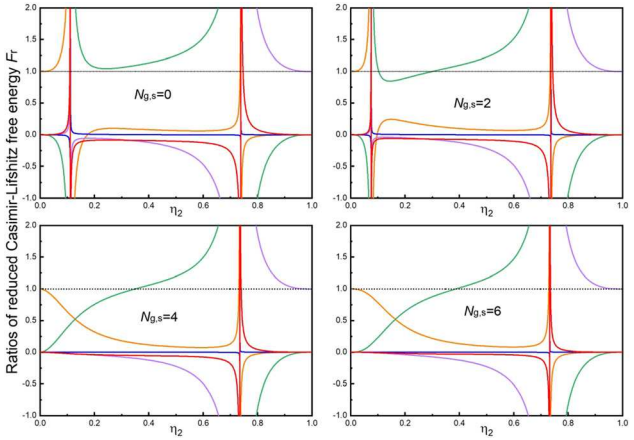

Fig. 12 Ratios of the contributions to the reduced Casimir–Lifshitz free energy $F_r = F_{CL} - F_{G_bG_sI} = F_{G_sIW} + F_{IWQ} + F_{G_bW} + F_{G_sQ} + F_{G_bQ}$ for the methane GH (bulk)-methane GH (surface)-ice–water–quartz (G_bG_sIWQ) configuration relative to the total. Namely, shown are the relative contributions of F_{G_sIW}/F_r (orange), F_{IWQ}/F_r (purple), F_{G_bW}/F_r (blue), F_{G_sQ}/F_r (green) and F_{G_bQ}/F_r (red), with various occupancy numbers $N_{g,s}$ of the 500 nm surface GH and the total thickness of ice and water layers is 1000 nm.

Moreover, for multi-layer contributions, their non-retarded forms, marked by their corresponding Hamaker constants, are influenced not just by the dielectric functions of materials involved as in three-layer cases, but also by the relative size of the intervening media. The dependence of Hamaker constants on the relative size of the ice layer in the configuration described by Fig. 3 and 4, is shown in detail in Fig. 11. As expected, when $\eta_2 = d_2/d$ approaches 0 or 1, the total Hamaker constant A goes to the three-layer contribution $\eta_2^{-2}A_{GIW}$ (red lines) or $\eta_3^{-2}A_{IWQ}$ (green lines). The pure four-layer interaction term A_{GQ} can only contribute in a limited way for the N_g = 0 and N_g = 4 cases, and would not change the sign of A, which is determined by $\eta_3^{-2}A_{IWQ}$. Since the permittivity of methane GH with the occupancy number N_g = 8 is between that of ice and water, more subtleties exist and are shown by the solid lines in Fig. 11. There is a section of η_2 (about 0.30 to 0.45) when N_g = 8, in which A_{GQ} has the magnitude comparable or even larger than two three-layer contributions. In this region, even a subtle balance, where a vanishing total Hamaker constant appears, can be achieved.

The case on the right in Fig. 11 (retarded), which shows the ratios of free energy for the same system with a relatively large total thickness of ice and water layers of 1000 nm thickness, is evidently different from the case on the left (non-retarded). As it has been seen on the left panel, when η_2 approaches 0 or 1, F_{GIW} or F_{IWQ} should dominate. However, with the retardation effects included, the purely four-layer contribution F_{GQ} could overwhelm three-layer contributions F_{GIW} and F_{IWQ} in a quite large range of η_2, for instance $0.2 < \eta_2 < 0.7$, which manifests the crucial role of the retardation effect in multi-layer interactions. Thus, it seems the non-retarded approximations are not very reliable in this case. However, the three-layer Hamaker constants have some merit providing predictions on formation of ice or water layers.

4.1.2 Analysis of energy contributions. The results in the previous sections were derived from careful computations of the free energy and stress for a large number of different inhomogeneous four-layer and five-layer geometries. As an example, we show in Fig. 9 the contour plots for a system with a 500 nm thick low-occupancy methane GH surface layer above the bulk methane GH. The equilibria, that is, the thicknesses of ice and water giving energy minima, depend on the distances between the GH and quartz. We observe that the thinner the GH surface layers are, the smaller the equilibrium thicknesses of the ice film will be. This is in line with the general results for multi-layered Casimir–Lifshitz interactions as discussed in the book by Parsegian.[55] For five-layer cases, the contributions to the reduced Casimir–Lifshitz free energies $F_r = F_{CL} - F_{G_bG_sI}$, obtained for inhomogeneous systems by omitting the contribution irrelevant to the thickness of ice layer, for the same configuration as in Fig. 9, are analysed in Fig. 12. Due to the four-layer interaction, F_{G_sQ} almost always dominates, while the other four-layer contributor F_{G_bW} is suppressed. There is an exception to the above, which occurs when the regularized free energy F_r vanishes due to cancellations between the various contributions. Three-layer contributions are significant only when η_2 approaches 0 or 1 as expected. The five-layer contribution is also typically small, but usually comparable with or even larger than the three-layer contributions.

4.2 Some general remarks on the role of ions

Here our focus is on systems where the stability of ice layers on methane gas hydrates within pores can be influenced. In previous sections, we predict that the effect of surface confinement, *via* Casimir–Lifshitz free energies in inhomogeneous systems, and the corresponding stresses, tends to reduce the thickness of anomalously stabilized ice layers, but also to

enhance the stabilising Casimir–Lifshitz free energy minima. While under specific conditions a dominating, and always contributing, role has been proposed for the Casimir–Lifshitz induced stresses across ice–water interface, another salt-dependent contribution[56–61] can induce destabilisation *via* repulsive forces for ice–water–quartz regions.

The Derjaguin–Landau–Verwey–Overbeek (DLVO) theory[62,63] for interactions between charged particles, or surfaces, in salt solutions treats colloid stability in terms of a balance of an attractive van der Waals force and a repulsive electrical double-layer force. An applied theory for salt-dependent forces in systems with ice–water–vapor was discussed a few years ago by Thiyam *et al.*[61] We focus in the current work on cases with high salt concentrations and/or pH near the isoelectric points (where surface charges are assumed close to zero), and the Casimir–Lifshitz interaction is dominating. It would be of interest in the future to address salt effects away from such specific limits (*e.g.* study cases with low salt concentrations,[61] varying pH,[61] or including different types of background salt ions[58,64]). A brief discussion on salt can be illuminating and indicate how salt is expected to influence the result. In order to quantify such additional contributions one must account for ions in water and the surface charges of ice, quartz, albite, and kaolinite. Some concentration of ions are always present in water, even in pure water due to autodissociation into H^+ and OH^- at pH 7. Autodissociation of water (ice) molecules at the ice–water interface (and correspondingly for quartz, albite and kaolinite) still takes place, generating an ice surface charge. Measurement of the zeta potential of the interfaces can be understood through a pH-dependent charge regulation model involving chemisorption of H^+ ions. When surface ice molecules dissociate at high pH, H^+ is liberated into solution leaving a negative charge due to OH^- remaining bound to the interface. At low pH, H^+ ions bind to surface molecules (analogous to forming an hydronium ion), resulting in a positive surface charge. The presence of surface charge induces physisorption of ion through electrostatic interactions. Physisorption can be modelled through a Poisson-Boltzmann model where the electrostatic potential of ions and surface charge is determined by solving the Poisson equation for the physisorbed ion concentration profiles[65] and chemisorbed surface charge.[60] Equilibrium physisorption profiles are described using a Boltzmann distribution determined from ion electrostatic energies. The free energy, and the force derived from the free energy, due to charge chemisorption and physisorption can be determined from the electrostatic energy of the electric field generated by the ions and surface charge, the entropic energy of ion concentration profiles,[66] and a charge transfer force.[60]

In the same way as when only Casimir–Lifshitz interactions are accounted for above, P_{23} is given by the difference of pressure across ice and pressure across salt water. One can then assume that the total stress across the water–ice interface can be approximated as,

$$P_{23} \simeq P_{\mathrm{CL},23} - P_{\mathrm{S},3}. \tag{18}$$

The corresponding free energy is approximately given by the sum of the five-layer Casimir–Lifshitz and ion free energies

$$F \simeq F_{\mathrm{CL}} + F_{\mathrm{S}}. \tag{19}$$

The zeta potentials for ice,[67] quartz[68] and albite,[68] as functions of salt concentration and pH, are all negative for pH 7, indicating negative surface charges. Usui[56,57] considered the salt induced pressure between a pair of surfaces with dissimilar electrostatic surface potentials both with same sign of the surface charge within the Gouy–Chapman–Stern–Grahame double-layer model. It was demonstrated that the double-layer force at low concentrations under surface charge regulation, was always repulsive between a pair of negatively charged surfaces, increasing with a decreasing surface separation.[56,57,59] These salt induced free energies are thus expected to promote growth of the liquid water layer. Since the total thickness of the ice and water layers is assumed fixed, this suggests melting of the ice layer. For low salt concentrations this effect is expected to dominate over the Lifshitz free energies. Hence, further studies away from the limits of high salt concentrations (*e.g.* sea salt) and/or pH at isoelectric points will be highly important expansions.

There can in fact also be effects of aqueous ions on the dielectric function of water, and therefore on the reflection coefficients used in the current work. This effect is known to be exceedingly small except at very high salt concentrations (exceeding 1 mol L^{-1}).[69] This is higher than the salt concentration of, for example, ocean water. Nevertheless, in general the possibility of tuning the formation of ice externally, or controlling the heat flux with an external electric field (which was studied for metal surfaces[70,71]) merits further study. One should note that a correction to the Casimir–Lifshitz interaction energy can occur, at high salt concentrations and/or thick water layers, due to screening of the zero frequency term by ions.[72–75] The impact of electrostatic energies of aqueous ions is usually more significant than the corresponding indirect impact on the Casimir–Lifshitz interaction.

5 Conclusions

It is well established that GHs containing a large fraction of methane molecules can exist under conditions of low temperatures and high pressures.[6] Such conditions may, for example, occur below the seabed and in deep permafrost layers. However, GHs have also been observed in shallow permafrost layers below the freezing point of water.[13] To be specific, ice layers covering methane GH surfaces have been associated with the stabilisation of GHs and believed to prevent the methane gas molecules from leaking out.[4–6]

In this work, we have demonstrated how Casimir–Lifshitz interactions at the quadruple point help to stabilize ice layer covers separating water from methane GHs inside porous rocks. Confinement effects are, within our Casimir–Lifshitz model, predicted to favor reduced ice layer thickness, compared to those of methane hydrates in larger reservoirs of ice cold

water.[15] Notably, while the self-preservation layers becomes thinner in pores, they may turn out to be more stable against perturbations compared to in larger water reservoirs.

Future work should further explore the potential environmental impacts from such stabilized gas hydrates. As was discussed in the introduction, Chuvilin, Shakhova and others,[11–13] have experimentally found that hydrates in permafrost regions seem to exist at very shallow depths from the surface. In fact, hydrates were found outside the expected pressure and temperature stability zone. For example Froitzheim *et al.*[76] reported observation of methane from particular rock types likely sourced from deep methane hydrates. The current investigation of GH self-preservation in pores is thus both relevant and important. Our study urgently calls for examining other relevant energy contributions, including those due to salt[61,77,78] and curvature,[79] as well as effects accounting for temperatures[23] below the quadruple point in future work.

Author contributions

Boström and Li designed the study. Berland performed *ab initio* DFT calculations for rock and clay materials. Brevik, and in parallel Fiedler, derived the five-layer Casimir–Lifshitz stress theory. Milton derived the general theory presented in the Appendix. Li, Esteso, and Carretero-Palacios performed the calculations for Casimir–Lifshitz interactions, as well as together with Boström analysing these results. Li analysed the results in terms of Hamaker contributions. Boström discussed contributions from ion induced interactions. All authors contributed to the writing and overall analysis of the manuscript. All authors have approved the final version of the manuscript.

Conflicts of interest

There are no conflicts of interest to declare.

Appendix

Casimir–Lifshitz interaction

Derivation of the Casimir–Lifshitz free energy for four-slab system

In this appendix, we use natural units, with $\hbar = c = k_B = 1$, and rationalized Heaviside–Lorentz electromagnetic units. We consider a 4-slab system, each slab being homogeneous:

$$\varepsilon,\mu(z) = \begin{cases} z < a: & \varepsilon_1, \mu_1, \\ a < z < b: & \varepsilon_2, \mu_2, \\ b < z < c: & \varepsilon_3, \mu_3, \\ c < z: & \varepsilon_4, \mu_4. \end{cases} \tag{20}$$

The free energy is given in general by

$$F = \frac{T}{2}\sum_{m=-\infty}^{\infty}\int\frac{\mathrm{d}^2k}{(2\pi)^2}\ln \Delta^{\mathrm{E}}\Delta^{\mathrm{H}}, \tag{21}$$

the sum being over Matsubara frequencies ζ_m, and E, H represent transverse electric (TE) and transverse magnetic (TM) polarizations, respectively. We will use the inhomogeneous medium description given by Li and co-workers.[48] We regard the regions 2 and 3 as a single region, labeled with "in", as an inhomogeneous medium. To obtain an unambigously finite result, we subtract a reference energy corresponding to removing the boundary a, that is, letting medium 2 to extend to $-\infty$. Then, we add back in the energy corresponding to that reference energy. So

$$F = F_{\mathrm{sub}} + F_{\mathrm{ref}}. \tag{22}$$

Here we consider the TE contribution only, the TM contribution being obtained by the obvious substitutions, E → H, $\varepsilon \leftrightarrow \mu$.

Consider first the reference situation, which is just the familiar DLP (three-layer) configuration. There

$$\Delta^{\mathrm{E}}_{\mathrm{ref}} = 1 - \frac{[e_{\overline{2},-}, e_{3,-}]_\mu(b)[e_{3,+}, e_{4,+}]_\mu(c)}{[e_{\overline{2},-}, e_{3,+}]_\mu(b)[e_{3,-}, e_{4,+}]_\mu(c)}, \tag{23}$$

where e_i satisfies

$$\left(\partial_z\frac{1}{\mu_i}\partial_z - \frac{k^2}{\mu_i} - \varepsilon_i\zeta^2\right)e_i = 0. \tag{24}$$

(The overline on the 2 is to remind us that region 2 has been extended to $-\infty$.) The generalized Wronskians are defined by

$$[e_i, e_j]_\mu = \frac{1}{\mu_i}e_i'e_j - \frac{1}{\mu_j}e_j'e_i, \tag{25}$$

evaluated at the same point. In this DLP configuration, we may define

$$e_{i,\pm} = e^{\mp\kappa_i z}, \quad \kappa_i = \sqrt{k^2 + \varepsilon_i\mu_i\zeta^2}. \tag{26}$$

Then it is immediate to find $\Delta^{\mathrm{E}}_{\mathrm{ref}} = \Delta^{\mathrm{E}}_{234}$, in which

$$\Delta^{\mathrm{E}}_{234} \equiv 1 - r^{\mathrm{E}}_{23}r^{\mathrm{E}}_{43}\mathrm{e}^{-2\kappa_3(c-b)}, \tag{27}$$

in terms of the reflection coefficients

$$r^{\mathrm{E}}_{ij} = \frac{\hat{\kappa}_j - \hat{\kappa}_i}{\hat{\kappa}_j + \hat{\kappa}_i}, \quad \hat{\kappa}_i = \frac{\kappa_i}{\mu_i}. \tag{28}$$

This directly gives the Casimir–Lifshitz energy and pressure.

Now for the subtracted four-slab configuration, we need to compute

$$\Delta^{\mathrm{E}}_{\mathrm{sub}} = 1 - \frac{[\mathrm{e}_{1,-}, \mathrm{e}_{\mathrm{in},-}]_\mu(a)[\mathrm{e}_{\mathrm{in},+}, \mathrm{e}_{4,+}]_\mu(c)}{[\mathrm{e}_{1,-}, \mathrm{e}_{\mathrm{in},+}]_\mu(a)[\mathrm{e}_{\mathrm{in},-}, \mathrm{e}_{4,+}]_\mu(c)}, \tag{29}$$

where the effort is only in finding the solution in the 2 + 3 region. We can take $\mathrm{e}_{\mathrm{in}\mp}(z)$ to be $\mathrm{e}^{\pm\kappa_2 z}$ for $a < z < b$; then by requiring, from the differential eqn (24), continuity of the solution, and of $\frac{1}{\mu}$ times the derivative of the solution, we find

$$e_{in,\mp}(z) = e^{\pm\kappa_2 z}, \quad a < z < b, \tag{30a}$$

while for $b < z < c$,

$$e_{in,\mp}(z) = \left[(\hat{\kappa}_3 - \hat{\kappa}_2)e^{\mp\kappa_3(z-b)} + (\hat{\kappa}_3 + \hat{\kappa}_2)e^{\pm\kappa_3(z-b)}\right]\frac{e^{\pm\kappa_2 b}}{2\hat{\kappa}_3}. \tag{30b}$$

Then Δ^{E}_{sub} is readily calculated to be

$$\Delta^{E}_{sub} = 1 + r^{E}_{12}e^{-2\kappa_2(b-a)}\frac{r^{E}_{23}e^{2\kappa_3(c-b)} + r^{E}_{34}}{e^{2\kappa_3(c-b)} + r^{E}_{34}r^{E}_{23}}. \tag{31}$$

When this is multiplied by Δ^{E}_{ref} in eqn (27), the denominator in eqn (32) is cancelled, and we are left with $\Delta^{E} = \Delta^{E}_{1234}$, in which

$$\Delta^{E}_{1234} \equiv 1 + r^{E}_{43}r^{E}_{32}e^{-2\kappa_3(c-b)} + r^{E}_{32}r^{E}_{21}e^{-2\kappa_2(b-a)} + r^{E}_{21}r^{E}_{43}e^{-2\kappa_2(b-a)}e^{-2\kappa_3(c-b)}. \tag{32}$$

Casimir–Lifshitz pressure on intermediate surface

We know that the principle of virtual work is satisfied in this formulation. Therefore, the force on the intermediate interface, b, between media 2 and 3, is

$$p_b = -\frac{\partial}{\partial b}T\sum_{m=0}^{\infty}{}'\sum_{s=E,H}\int\frac{d^2k}{(2\pi)^2}\ln\Delta^{s}. \tag{33}$$

Here,

$$\frac{\partial}{\partial b}\ln\Delta^{s} = \frac{2\kappa_2}{D^{s}_{2}} - \frac{2\kappa_3}{D^{s}_{3}}, \tag{34}$$

where, after a bit of rearrangement,

$$D^{s}_{3} = -1 - \frac{e^{2\kappa_3(c-b)}}{r^{s}_{43}\bar{r}^{s}_{32}}, \quad D^{s}_{2} = -1 - \frac{e^{2\kappa_2(b-a)}}{r^{s}_{12}\bar{r}^{s}_{23}}, \tag{35}$$

and the effect of the fourth medium is absorbed in the effective reflection coefficients

$$\bar{r}^{s}_{32} = \frac{r^{s}_{32} + r^{s}_{21}e^{-2\kappa_2(b-a)}}{1 + r^{s}_{32}r^{s}_{21}e^{-2\kappa_2(b-a)}}, \quad \bar{r}^{s}_{23} = \frac{r^{s}_{23} + r^{s}_{34}e^{-2\kappa_3(c-b)}}{1 + r^{s}_{23}r^{s}_{34}e^{-2\kappa_3(c-b)}}. \tag{36}$$

Casimir–Lifshitz theory with n intervening slabs

Let us generalize the above considerations to the situation with n homogeneous layers sandwiched between two semi-infinite bulks. The situation is illustrated in Fig. 13.

The free energy is still given by eqn (21), and to obtain a finite energy we subtract the reference situation, which would now be given by letting the region 1 extend to $-\infty$, that is, eliminate the boundary a, which gives the $n-1$ intermediate slab configuration. The subtracted Δ is given by the generalization of eqn (29),

$$\Delta^{E}_{sub} = 1 - \frac{[e_{L,-}, e_{in,-}]_{\mu}(a)[e_{in,+}, e_{R,+}]_{\mu}(c)}{[e_{L,-}, e_{in,+}]_{\mu}(a)[e_{in,-}, e_{R,+}]_{\mu}(c)}, \tag{37}$$

In the outer slabs, we take $\left(\kappa_i = \sqrt{k^2 + \zeta_m^2\varepsilon_i(\zeta_m)\mu_i(\zeta_m)}\right)$

$$e_{L,-} = e^{\kappa_L z}, \quad e_{R,+} = e^{-\kappa_R z}, \tag{38}$$

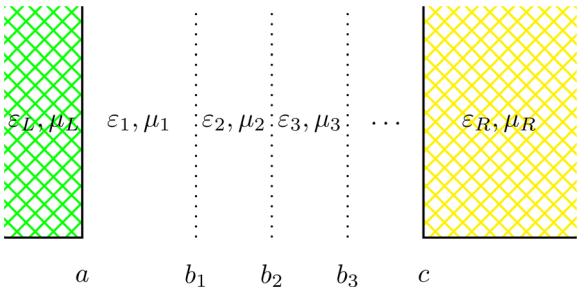

Fig. 13 Geometry of n homogeneous parallel slabs, with interfaces at b_i, $i = 0,1,2,\ldots,n,n+1$, with permittivity ε_i and permeability μ_i in the $i > 0$ th slab. These slabs are sandwiched between two parallel semi-infinite media, where for $z < a$, the permittivity and permeability are ε_L, μ_L, and for $z > c$, the permittivity and permeability are $\varepsilon_{n+1} = \varepsilon_R$, $\mu_{n+1} = \mu_R$, where $a = b_0 < b_1 < b_2 < \ldots < b_n < b_{n+1} = c$.

while in the first interior slab, we may take

$$e_{1,\mp} = e^{\pm\kappa_1 z}, \quad a < z < b_1, \tag{39}$$

while e_{in} in the remaining slabs can be written as

$$e_{in,\mp}(z) = A_i^{\pm}e^{\kappa_i z} + B_i^{\pm}e^{-\kappa_i z}, \quad b_{i-1} < z < b_i, \tag{40}$$

where $A_1^{+} = 1$, $A_1^{-} = 0$, $B_1^{+} = 0$, $B_1^{-} = 1$, and the coefficients are obtained by the continuity of the function, and of $1/\mu$ times the derivative of the function, at the interfaces. These matching conditions can be written in matrix form:

$$\mathbf{M}_{i+1}\psi^{\pm}_{i+1} = \mathbf{N}_i\psi^{\pm}_i, \ \psi^{\pm}_i = \begin{pmatrix} A^{\pm}_i \\ B^{\pm}_i \end{pmatrix}, \tag{41}$$

with the matrices

$$\mathbf{M}_{i+1} = \begin{pmatrix} e^{\kappa_{i+1}b_i} & e^{-\kappa_{i+1}b_i} \\ \hat{\kappa}_{i+1}e^{\kappa_{i+1}b_i} & -\hat{\kappa}_{i+1}e^{-\kappa_{i+1}b_i} \end{pmatrix}, \quad \mathbf{N}_i = \begin{pmatrix} e^{\kappa_i b_i} & e^{-\kappa_i b_i} \\ \hat{\kappa}_i e^{\kappa_i b_i} & -\hat{\kappa}_i e^{-\kappa_i b_i} \end{pmatrix}, \tag{42}$$

and then in terms of the transfer matrix

$$\mathbf{T}_i = \mathbf{M}_i^{-1}\mathbf{N}_{i-1} = \frac{1}{2\kappa_i}\begin{bmatrix} (\kappa_i + \kappa_{i-1})e^{-(\kappa_i-\kappa_{i-1})b_{i-1}} & (\kappa_i - \kappa_{i-1})e^{-(\kappa_i+\kappa_{i-1})b_{i-1}} \\ (\kappa_i - \kappa_{i-1})e^{(\kappa_i+\kappa_{i-1})b_{i-1}} & (\kappa_i - \kappa_{i-1})e^{(\kappa_i-\kappa_{i-1})b_{i-1}} \end{bmatrix}, \tag{43}$$

we have for the amplitude in the last intermediate slab

$$\psi^{\pm}_n = \mathbf{T}_n\mathbf{T}_{n-1}\mathbf{T}_{n-2}\cdots\mathbf{T}_2\psi^{\pm}_1, \quad \psi^{+}_1 = \begin{pmatrix} 1 \\ 0 \end{pmatrix}, \psi^{-}_1 = \begin{pmatrix} 0 \\ 1 \end{pmatrix}. \tag{44}$$

This multiplicative structure makes it easy to go from the result for n layers to that for $n+1$ layers.

Using this machinery, let's write down the basis function in the 3rd intermediate slab for the five-layer system:

$$\begin{aligned} e_{in,-}(z) &= \frac{\hat\kappa_1+\hat\kappa_2}{2\hat\kappa_2}\frac{\hat\kappa_2+\hat\kappa_3}{2\hat\kappa_3}e^{\kappa_1 b_1}e^{\kappa_2(b_2-b_1)}\Big\{\Big[1+r_{12}r_{23}e^{-2\kappa_2(b_2-b_1)}\Big] \\ &\quad\times e^{\kappa_3(z-b_2)}+\Big[r_{23}+r_{12}e^{-2\kappa_2(b_2-b_1)}\Big]e^{-\kappa_3(z-b_2)}\Big\}, \\ &\quad b_2<z<c, \end{aligned} \tag{45a}$$

$$\begin{aligned} e_{in,+}(z) &= \frac{\hat\kappa_1+\hat\kappa_2}{2\hat\kappa_2}\frac{\hat\kappa_2+\hat\kappa_3}{2\hat\kappa_3}e^{-\kappa_1 b_1}e^{\kappa_2(b_2-b_1)}\Big\{\Big[r_{12}+r_{23}e^{-2\kappa_2(b_2-b_1)}\Big] \\ &\quad\times e^{\kappa_3(z-b_2)}+\Big[r_{23}r_{12}+e^{-2\kappa_2(b_2-b_1)}\Big]e^{-\kappa_3(z-b_2)}\Big\}, \\ &\quad b_2<z<c. \end{aligned} \tag{45b}$$

We can check these results by noting that if $r_{23} = 0$ and $\kappa_3 = \kappa_2$ this reduces to the formula (30b) for the two intermediate slab situation.

We can now readily compute the $\Delta^{\mathrm{E}}_{\mathrm{sub}}$ from the Wronskians in eqn (37). The denominator that appears is precisely cancelled by multiplying the 4-slab Δ given in eqn (32), with suitable notation changes. The result $\Delta^E = \Delta^{\mathrm{E}}_{\mathrm{sub}}\Delta^{\mathrm{E}}_{\mathrm{ref}}$ is actually very simple, and can be readily interpreted:

$$\begin{aligned} \Delta^{\mathrm{E}} &= 1+r^{\mathrm{E}}_{\mathrm{L}1}r^{\mathrm{E}}_{12}E^{-2\kappa_1(b_1-a)}+r^{\mathrm{E}}_{12}r^{\mathrm{E}}_{23}e^{-2\kappa_2(b_2-b_1)}+r^{\mathrm{E}}_{23}r^{\mathrm{E}}_{3\mathrm{R}}e^{-2\kappa_3(c-b_2)} \\ &\quad+r^{\mathrm{E}}_{\mathrm{L}1}r^{\mathrm{E}}_{23}e^{-2\kappa_1(b_1-a)}e^{-2\kappa_2(b_2-b_1)}+r^{\mathrm{E}}_{12}r^{\mathrm{E}}_{3\mathrm{R}}e^{-2\kappa_2(b_2-b_1)}e^{-2\kappa_3(c-b_2)} \\ &\quad+r^{\mathrm{E}}_{\mathrm{L}1}r^{\mathrm{E}}_{12}r^{\mathrm{E}}_{23}r^{\mathrm{E}}_{3\mathrm{R}}e^{-2\kappa_1(b_1-a)}e^{-2\kappa_3(c-b_2)} \\ &\quad+r^{\mathrm{E}}_{\mathrm{L}1}r^{\mathrm{E}}_{3\mathrm{R}}e^{-2\kappa_1(b_1-a)}e^{-2\kappa_2(b_2-b_1)}e^{-2\kappa_3(c-b_2)}. \end{aligned} \tag{46}$$

We can check this result by verifying that this gives the correct pressure across the interfaces. For example, the pressure on the b_2 interface is

$$p_{b_2} = T_{zz}(b_2-) - T_{zz}(b_2+) = -\frac{\partial}{\partial b_2}T{\sum_{m=0}^{\infty}}'\sum_{s=E,H}\int\frac{\mathrm{d}^2k}{(2\pi)^2}\ln\Delta^s, \tag{47}$$

where, for example,

$$\frac{\partial}{\partial b_2}\ln\Delta^{\mathrm{E}} = \frac{2\kappa_2}{D^{\mathrm{E}}_2}-\frac{2\kappa_3}{D^{\mathrm{E}}_3}, \tag{48}$$

with

$$D^{\mathrm{E}}_2 = \frac{1}{\bar r^{\mathrm{E}}_{23}\bar r^{\mathrm{E}}_{21}}e^{2\kappa_2(b_2-b_1)}-1, \tag{49a}$$

$$D^{\mathrm{E}}_3 = \frac{1}{r^{\mathrm{E}}_{3\mathrm{R}}\bar r^{\mathrm{E}}_{32}}e^{2\kappa_3(c-b_2)}-1, \tag{49b}$$

where the multiple scattered reflection coefficients are

$$\bar r^{\mathrm{E}}_{23} = \frac{r^{\mathrm{E}}_{23}+r^{\mathrm{E}}_{3\mathrm{R}}e^{-2\kappa_3(c-b_2)}}{1+r^{\mathrm{E}}_{23}r^{\mathrm{E}}_{3\mathrm{R}}e^{-2\kappa_3(c-b_2)}}, \tag{50a}$$

$$\bar r^{\mathrm{E}}_{21} = \frac{r^{\mathrm{E}}_{21}+r^{\mathrm{E}}_{1\mathrm{L}}e^{-2\kappa_1(b_1-a)}}{1+r^{\mathrm{E}}_{21}r^{\mathrm{E}}_{1\mathrm{L}}e^{-2\kappa_1(b_1-a)}}, \tag{50b}$$

$$\bar r^{\mathrm{E}}_{32} = \frac{r^{\mathrm{E}}_{32}+\bar r^{\mathrm{E}}_{21}e^{-2\kappa_2(b_2-b_1)}}{1+r^{\mathrm{E}}_{32}\bar r^{\mathrm{E}}_{21}e^{-2\kappa_2(b_2-b_1)}}. \tag{50c}$$

This agrees with the results of Ellingsen[46] and Buhmann.[50] Analogous results hold for the TM modes. These results are used in the calculations in this paper after a simple replacement: $b_1-a \to d_1$, $b_2-b_1 \to d_2$, and $c-b_2 \to d_3$.

On the other hand, by regarding the regions 1, 2 and 3 as a single inhomogeneous medium, then we obtain the interaction Casimir free energy between L-1 and 3-R surfaces F_{LR}

$$F_{\mathrm{LR}} = \frac{T}{2}\sum_{m=-\infty}^{\infty}\int\frac{\mathrm{d}^2k}{(2\pi)^2}\ln\Delta^{\mathrm{E}}_{\mathrm{LR}}\Delta^{\mathrm{H}}_{\mathrm{LR}}, \tag{51}$$

in which Δ^s_{LR},s = E,H is written as

$$\Delta^s_{\mathrm{LR}} = 1+\frac{r^s_{\mathrm{L}1}(1-r_{12}{}^{s2})(1-r_{23}{}^{s2})r^s_{3R}}{\Delta^s_{\mathrm{L}123}\Delta^s_{123R}}e^{-2(\kappa_1 d_1+\kappa_2 d_2+\kappa_3 d_3)}. \tag{52}$$

The total Casimir free energy of this five-layer system F can be expressed as $F = F_{\mathrm{LR}} + F_{\mathrm{L}123} + F_{123R} - F_{123}$, in which F_{LR} results from the pure five-layer interaction.

Interpretation of nonhomogeneous Lifshtz theory

Although the energy forms are quite simple, they are not quite so obvious from a geometrical point of view. The interpretation of the force expressions are quite simple, in contrast, because of the locality of the stess tensor. We can follow the multiple reflection argument given in ref. 80 to write down the form of the reduced Green's function (for a given frequency and wavenumber) in the ith slab for a given scalar mode, for $b_{i-1} < z, z' < b_i$:

$$\begin{aligned} g(z,z') &= \frac{1}{2\kappa_i}\Big\{e^{-\kappa_i|z-z'|}+\Big[e^{2\kappa_i(b_i-b_{i-1})}-\bar r_{i,i+1}\bar r_{i,i-1}\Big]^{-1} \\ &\quad\times\Big[2\bar r_{i,i-1}\bar r_{i,i+1}\cosh\kappa_i(z-z') \\ &\quad+\bar r_{i,i+1}e^{\kappa_i(z+z'-2b_{i-1})}+\bar r_{i,i-1}e^{-\kappa_i(z+z'-2b_i)}\Big]\Big\}. \end{aligned} \tag{53}$$

(This multi-layer Green's function was first obtained by Tomaš.[45] See also the book by Chew.[81]) The reduced stress tensor is given by

$$t_{zz} = \frac{1}{2}(\partial_z\partial_{z'}-\kappa^2)\frac{1}{i}g(z,z')|_{z=z'}, \tag{54}$$

which annihilates all but the hyperbolic cosine, and yields immediately for Euclidean frequencies

$$t_{zz}(b_i-) = -\frac{2\kappa_i}{D_i}, \quad t_{zz}(b_i+) = -\frac{2\kappa_{i+1}}{D_{i+1}}, \tag{55}$$

where

$$D_i = \frac{1}{\bar r_{i,i+1}}\frac{1}{\bar r_{i,i-1}}e^{2\kappa_i(b_i-b_{i-1})}-1. \tag{56}$$

which implies eqn (47).

As for the effective reflection coefficients appearing here, in terms of reflection and transmission coefficients we see by

considering multiple reflections from the right, ($d_{i+1} = b_{i+1} - b_i$)

$$\begin{aligned}\bar{r}_{i,i+1} &= r_{i,i+1} + t_{i,i+1}e^{-\kappa_{i+1}d_{i+1}}\bar{r}_{i+1,i+2}e^{-\kappa_{i+1}d_{i+1}}t_{i+1,i} \\ &\quad + t_{i,i+1}e^{-\kappa_{i+1}d_{i+1}}\bar{r}_{i+1,i+2}e^{-\kappa_{i+1}d_{i+1}}r_{i+1,i}e^{-\kappa_{i+1}d_{i+1}}\bar{r}_{i+1,i+2} \\ &\quad \times e^{-\kappa_{i+1}d_{i+1}}t_{i+1,i} + \ldots \\ &= r_{i,i+1} + t_{i+1,i}t_{i,i+1}\frac{1}{r_{i,i+1}}\frac{1}{1 - \frac{1}{r_{i+1,i}}\frac{1}{\bar{r}_{i+1,i+2}}e^{2\kappa_{i+1}d_{i+1}}}.\end{aligned} \tag{57}$$

Here, the transmission coefficients are related to the reflection coefficients by $t_{ij} = 1 + r_{ij}$, so because for the primitive reflection coefficients, $r_{ij} = -r_{ji}$, $t_{i+1,i}t_{i,i+1} = 1 - r_{i,i+1}{}^2$ and so

$$\bar{r}_{i,i+1} = \frac{r_{i,i+1}e^{2\kappa_{i+1}d_{i+1}} + \bar{r}_{i+1,i+2}}{e^{2\kappa_{i+1}d_{i+1}} + r_{i,i+1}\bar{r}_{i+1,i+2}}. \tag{58}$$

Similarly, for the reflection coefficients on the left:

$$\bar{r}_{i,i-1} = \frac{r_{i,i-1}e^{2\kappa_{i-1}d_{i-1}} + \bar{r}_{i-1,i-2}}{e^{2\kappa_{i-1}d_{i-1}} + r_{i,i-1}\bar{r}_{i-1,i-2}}. \tag{59}$$

Here, for the first and last slabs, the distinction between r and $\bar{r}$ disappears:

$$\bar{r}_{n,\mathrm{R}} = r_{n,\mathrm{R}}, \quad \bar{r}_{1,\mathrm{L}} = r_{1,\mathrm{L}}. \tag{60}$$

Thin-thickness limits

Suppose the thickness of one of the intervening layers, say medium i as depicted in Fig. 13, vanishes ($d_i = 0$), then $\bar{r}_{i+1,i}$ can be expressed as

$$\begin{aligned}\bar{r}_{i+1,i} &= \frac{r_{i+1,i}(e^{2\kappa_{i-1}d_{i-1}} + r_{i,i-1}\bar{r}_{i-1,i-2}) + r_{i,i-1}e^{2\kappa_{i-1}d_{i-1}} + \bar{r}_{i-1,i-2}}{e^{2\kappa_{i-1}d_{i-1}} + r_{i,i-1}\bar{r}_{i-1,i-2} + r_{i+1,i}(r_{i,i-1}e^{2\kappa_{i-1}d_{i-1}} + \bar{r}_{i-1,i-2})} \\ &= \frac{r_{i+1,i-1}e^{2\kappa_{i-1}d_{i-1}} + \bar{r}_{i-1,i-2}}{e^{2\kappa_{i-1}d_{i-1}} + r_{i+1,i-1}\bar{r}_{i-1,i-2}} \equiv \bar{r}_{i+1,i-1},\end{aligned} \tag{61}$$

and similarly $\bar{r}_{i-1,i}$ takes the form

$$\begin{aligned}\bar{r}_{i-1,i} &= \frac{r_{i-1,i}(e^{2\kappa_{i+1}d_{i+1}} + r_{i,i+1}\bar{r}_{i+1,i+2}) + r_{i,i+1}e^{2\kappa_{i+1}d_{i+1}} + \bar{r}_{i+1,i+2}}{e^{2\kappa_{i+1}d_{i+1}} + r_{i,i+1}\bar{r}_{i+1,i+2} + r_{i-1,i}(r_{i,i+1}e^{2\kappa_{i+1}d_{i+1}} + \bar{r}_{i+1,i+2})} \\ &= \frac{r_{i-1,i+1}e^{2\kappa_{i+1}d_{i+1}} + \bar{r}_{i+1,i+2}}{e^{2\kappa_{i+1}d_{i+1}} + r_{i-1,i+1}\bar{r}_{i+1,i+2}} \equiv \bar{r}_{i-1,i+1}.\end{aligned} \tag{62}$$

Here, we have defined for the vanishingly thin slab the effective reflection coefficients

$$r_{i+1,i-1} = \frac{r_{i+1,i} + r_{i,i-1}}{1 + r_{i+1,i}r_{i,i-1}}, \quad r_{i-1,i+1} = \frac{r_{i-1,i} + r_{i,i+1}}{1 + r_{i-1,i}r_{i,i+1}}. \tag{63}$$

Therefore, in this limiting case, the pressures on other interfaces are obtained just as though the medium i has never existed. The only subtleties come from the vanishing layer, which will typically give rise to divergences in its own Casimir–Lifshitz free energy and corresponding pressure. We will not go deeper into the interpretation of this vanishing layer at this point.

We can subtract the effects of the vanishing layer from the Casimir–Lifshitz free energy. To be more specific and relevant, consider the four- and five-layer cases as in the main text. For the 1–2–3–4 structure as described by eqn (32), when the medium 2 has vanishing thickness ($d_2 = b - a \to 0$), the total Casimir–Lifshitz free energy can be subtracted, leaving for the remaining parts $F_\mathrm{r} = F - F_{123}$, which means the corresponding "renormalized" factor Δ^s_reg is

$$\Delta^s_\mathrm{reg} = \frac{\Delta^s_{1234}}{\Delta^s_{123}} = 1 + r^s_{43}\bar{r}^s_{32}e^{-2\kappa_3(c-b)}, \tag{64}$$

which means that, with $b-a = 0$ and $\bar{r}^s_{32} = r^s_{32}$, this four-layer structure is reduced to the well-known three-layer case. For the five-layer case L-1-2-3-R, with the thickness of medium 1 being zero, the regularized factor is just that of the four-layer case L-2-3-R, $\Delta^s_\mathrm{reg} = \Delta^s_{\mathrm{L123R}}/\Delta_{\mathrm{L12}} = \Delta^s_{\mathrm{L23R}}$.

Acknowledgements

We especially thank Fabian Spallek for independent tests of the relevant reflection coefficients as well as providing useful comments on our manuscript. We thank Dr Drew F. Parsons for discussions on the role of ion free energies. We would also like to thank Juan Luengo Márquez and Dr Luis G. MacDowell who shared their independently prepared files with dielectric function data[22,23] for ice and water. We thank the Terahertz Physics and Devices Group, Nanchang University. for the strong computational facility support. The DFT computations in this work were funded by The Norwegian e-Infrastructure for Research and Education, Sigma2, through grants No. NN9650k. The research of SCP was supported in part by the National Science Foundation under Grant No. NSF PHY-1748958. The work of KAM was supported in part by a grant from the US National Science Foundation, No. 2008417. The authors thank the "ENSEMBLE3 - Centre of Excellence for nanophotonics, advanced materials and novel crystal growth-based technologies" project (GA No. MAB/2020/14) carried out within the International Research Agendas programme of the Foundation for Polish Science co-financed by the European Union under the European Regional Development Fund and the European Union's Horizon 2020 research and innovation programme Teaming for Excellence (GA. No. 857543) for support of this work.

Notes and references

1 Y. Handa, *J. Chem. Thermo.*, 1986, **18**, 891–902.
2 A. Hallbrucker and E. Mayer, *J. Chem. Soc., Faraday Trans.*, 1990, **86**, 3785–3792.
3 E. Ershov and V. Yakushev, *Cold Reg. Sci. Technol.*, 1992, **20**, 147–156.
4 S. Takeya and J. Ripmeester, *Angew. Chem., Int. Ed.*, 2008, **47**, 1276–1279.

5 A. Falenty and W. F. Kuhs, *J. Phys. Chem. B*, 2009, **113**, 15975–15988.
6 A. Hachikubo, S. Takeya, E. Chuvilin and V. Istomin, *Phys. Chem. Chem. Phys.*, 2011, **13**, 17449–17452.
7 A. Falenty, W. F. Kuhs, M. Glockzin and G. Rehder, *Energy Fuels*, 2014, **28**, 6275–6283.
8 W. F. Kuhs, G. Genov, D. K. Staykova and T. Hansen, *Phys. Chem. Chem. Phys.*, 2004, **6**, 4917–4920.
9 P. S. R. Prasad and B. S. Kiran, *Sci. Rep.*, 2019, **9**, 5860.
10 C. D. Ruppel and J. D. Kessler, *Rev. Geophys.*, 2017, **55**, 126–168.
11 N. Shakhova, I. Semiletov, O. Gustafsson, V. Sergienko, L. Lobkovsky, O. Dudarev, V. Tumskoy, M. Grigoriev, A. Mazurov, A. Salyuk, R. Ananiev, A. Koshurnikov, D. Kosmach, A. Charkin, N. Dmitrevsky, V. Karnaukh, A. Gunar, A. Meluzov and D. Chernykh, *Nat. Commun.*, 2017, **8**, 15872.
12 E. Chuvilin, B. Bukhanov, D. Davletshina, S. Grebenkin and V. Istomin, *Geosciences*, 2018, **8**, 431.
13 N. Shakhova, I. Semiletov and E. Chuvilin, *Geosciences*, 2019, **9**, 251.
14 M. Boström, R. W. Corkery, E. R. A. Lima, O. I. Malyi, S. Y. Buhmann, C. Persson, I. Brevik, D. F. Parsons and J. Fiedler, *ACS Earth Space Chem.*, 2019, **3**, 1014–1022.
15 M. Boström, V. Esteso, J. Fiedler, I. Brevik, S. Y. Buhmann, C. Persson, S. Carretero-Palacios, D. F. Parsons and R. W. Corkery, *Astron. Astrophys.*, 2021, **650**, A54.
16 S. Kamata, F. Nimmo, Y. Sekine, K. Kuramoto, N. Noguchi, J. Kimura and A. Tani, *Nat. Geosci.*, 2019, **12**, 407–410.
17 E. Sloan Jr. and C. Koh, *Clathrate Hydrates of Natural Gases*, CRC Press, Boca Raton, 2007.
18 J. Fiedler, M. Boström, C. Persson, I. H. Brevik, R. W. Corkery, S. Y. Buhmann and D. F. Parsons, *J. Phys. Chem. B*, 2020, **124**, 3103–3113.
19 M. Elbaum and M. Schick, *Phys. Rev. Lett.*, 1991, **66**, 1713–1716.
20 M. Elbaum and M. Schick, *J. Phys. I France*, 1991, **1**, 1665–1668.
21 Y. Li, K. A. Milton, I. Brevik, O. I. Malyi, P. Thiyam, C. Persson, D. F. Parsons and M. Boström, *Phys. Rev. B*, 2022, **105**, 014203.
22 J. Luengo-Márquez and L. G. MacDowell, *J. Coll. Interf. Sci.*, 2021, **590**, 527–538.
23 J. Luengo-Márquez, F. Izquierdo-Ruiz and L. G. MacDowell, *J. Chem. Phys.*, 2022, **157**, 044704.
24 G. Kresse and J. Hafner, *Phys. Rev. B: Condens. Matter Mater. Phys.*, 1993, **47**, 558–561.
25 G. Kresse and J. Furthmüller, *Comput. Mat. Sci.*, 1996, **6**, 15–50.
26 G. Kresse and J. Furthmüller, *Phys. Rev. B: Condens. Matter Mater. Phys.*, 1996, **54**, 11169–11186.
27 albite (NaAlSi3O8 rt, T= 93 K) Crystal Structure: Datasheet from ''PAULING FILE Multinaries Edition-2012'' in Springer Materials, **https://materials.springer.com/isp/crystallographic/docs/sd_1811945**, accessed 2021-12-16.
28 quartz (SiO_2 rt) Crystal Structure: Datasheet from ''PAULING FILE Multinaries Edition-2012'' in Springer Materials, **https://materials.springer.com/isp/crystallographic/docs/sd_1520590**, accessed 2021-12-16.
29 kaolinite (Al2Si2O5[OH]4 kao) Crystal Structure: Datasheet from ''PAULING FILE Multinaries Edition-2012'' in Springer Materials, **https://materials.springer.com/isp/crystallographic/docs/sd_1214539**, accessed 2021-12-16.
30 J. Heyd, G. E. Scuseria and M. Ernzerhof, *J. Chem. Phys.*, 2003, **118**, 8207–8215.
31 J. Heyd, G. E. Scuseria and M. Ernzerhof, *J. Chem. Phys.*, 2003, **118**, 8207–8215.
32 D. E. Aspnes, *Am. J. Phys.*, 1982, **50**, 704–709.
33 O. Bonnefoy, F. Gruy and J.-M. Herri, *Mat. Chem. Phys.*, 2005, **89**, 336–344.
34 O. Bonnefoy, F. Gruy and J.-M. Herri, *Fluid Phase Equilib.*, 2005, **231**, 176–187.
35 In *CRC Handbook of Chemistry and Physics*, ed. D. R. Linde, CRC Press, Boca Raton (FL), 86th edn, 2005.
36 O. Prieto-Ballesteros, J. S. Kargel, M. Fernandez-Sampedro, F. Selsis, E. S. Martinez and D. L. Hogenboom, *Icarus*, 2005, **177**, 491–505.
37 J. Fiedler, P. Thiyam, A. Kurumbail, F. A. Burger, M. Walter, C. Persson, I. Brevik, D. F. Parsons, M. Boström and S. Y. Buhmann, *J. Phys. Chem. A*, 2017, **121**, 9742–9751.
38 D. Parsons and B. W. Ninham, *Langmuir*, 2010, **26**, 1816–1823.
39 I. Dzyaloshinskii, E. Lifshitz and L. Pitaevskii, *Adv. Phys.*, 1961, **10**, 165–209.
40 V. A. Parsegian and B. W. Ninham, *Nature*, 1969, **224**, 1197–1198.
41 B. Ninham and V. Parsegian, *Biophys. J.*, 1970, **10**, 646–663.
42 P. Richmond and B. Ninham, *Solid State Comm.*, 1971, **9**, 1045–1047.
43 P. Richmond and B. W. Ninham, *J. Phys. C-Solid State Phys.*, 1971, **4**, 1988–1993.
44 V. Esteso, S. Carretero-Palacios, L. G. MacDowell, J. Fiedler, D. F. Parsons, F. Spallek, H. Míguez, C. Persson, S. Y. Buhmann, I. Brevik and M. Boström, *Phys. Chem. Chem. Phys.*, 2020, **22**, 11362–11373.
45 M. S. Tomaš, *Phys. Rev. A*, 1995, **51**, 2545–2559.
46 S. A. Ellingsen, *J. Phys. A: Math. Theor.*, 2007, **40**, 1951–1961.
47 P. Parashar, K. A. Milton, Y. Li, H. Day, X. Guo, S. A. Fulling and I. Cavero-Peláez, *Phys. Rev. D*, 2018, **97**, 125009.
48 Y. Li, K. A. Milton, X. Guo, G. Kennedy and S. A. Fulling, *Phys. Rev. D*, 2019, **99**, 125004.
49 J. Fiedler, F. Spallek, P. Thiyam, C. Persson, M. Boström, M. Walter and S. Y. Buhmann, *Phys. Rev. A*, 2019, **99**, 062512.
50 S. Y. Buhmann, *Dispersion Forces I: Macroscopic quantum electrodynamics and ground-state Casimir, Casimir-Polder and van der Waals forces*, Springer, Heidelberg, 2012.
51 J. Fiedler, K. Berland, F. Spallek, I. Brevik, C. Persson, S. Y. Buhmann and M. Boström, *Phys. Rev. B*, 2020, **101**, 235424.
52 D. B. Hough and L. R. White, *Adv. Coll. Interf. Sci.*, 1980, **14**, 3–41.
53 L. Bergström, *Adv. Coll. Interf. Sci.*, 1997, **70**, 125–169.

54 V. Esteso, S. Carretero-Palacios and H. Míguez, *Phys. Rev. A*, 2020, **101**, 033815.
55 V. A. Parsegian, *van der Waals forces: A handbook for biologists, chemists, engineers, and physicists*, Cambridge University Press, New York, 2006.
56 S. Usui, *J. Coll. Interf. Sci.*, 2004, **280**, 113–119.
57 D. Y. Chan, T. W. Healy, T. Supasiti and S. Usui, *J. Coll. Interf. Sci.*, 2006, **296**, 150–158.
58 D. F. Parsons, M. Boström, P. L. Nostro and B. W. Ninham, *Phys. Chem. Chem. Phys.*, 2011, **13**, 12352–12367.
59 G. Trefalt, F. J. M. Ruiz-Cabello and M. Borkovec, *J. Phys. Chem. B*, 2014, **118**, 6346–6355.
60 D. F. Parsons and A. Salis, *J. Chem. Phys.*, 2015, **142**, 134707.
61 P. Thiyam, J. Fiedler, S. Y. Buhmann, C. Persson, I. Brevik, M. Boström and D. F. Parsons, *J. Phys. Chem. C*, 2018, **122**, 15311–15317.
62 B. V. Deryaguin and L. Landau, *Acta Phys. Chem.*, 1941, **14**, 633.
63 E. J. W. Verwey and J. T. G. Overbeek, *Theory of the Stability of Lyophobic Colloids*, Elsevier, Amsterdam, 1948.
64 M. Boström, D. R. M. Williams and B. W. Ninham, *Phys. Rev. Lett.*, 2001, **87**, 168103.
65 D. F. Parsons and B. W. Ninham, *J. Phys. Chem. C*, 2012, **116**, 7782–7792.
66 J. Theodoor and G. Overbeek, *Colloids Surf.*, 1990, **51**, 61–75.
67 N. Kallay, A. Čop, E. Chibowski and L. Holysz, *J. Coll. Interf. Sci.*, 2003, **259**, 89–96.
68 L. O. Filippov, A. Duverger, I. V. Filippova, H. Kasaini and J. Thiry, *Miner. Eng.*, 2012, **36–38**, 314–323.
69 R. A. Robinson and R. H. Stokes, *Electrolyte Solutions*, Butterworths Scientific Publications, 2nd edn, 1959.
70 A. I. Volokitin, *JETP Lett.*, 2019, **109**, 749–754.
71 A. I. Volokitin and B. N. J. Persson, *J. Condens. Matter Phys.*, 2020, **32**, 255301.
72 B. W. Ninham and V. Yaminsky, *Langmuir*, 1997, **13**, 2097–2108.
73 B. W. Ninham, M. Boström, C. Persson, I. Brevik, S. Y. Buhmann and B. E. Sernelius, *Eur. Phys. J. D*, 2014, **68**, 328.
74 P. A. Maia Neto, F. S. S. Rosa, L. B. Pires, A. B. Moraes, A. Canaguier-Durand, R. Guérout, A. Lambrecht and S. Reynaud, *Eur. Phys. J. D*, 2019, **73**, 178.
75 R. O. Nunes, B. Spreng, R. de Melo e Souza, G.-L. Ingold, P. A. Maia Neto and F. S. Rosa, *Universe*, 2021, **7**, 156.
76 N. Froitzheim, J. Majka and D. Zastrozhnov, *Proc. Natl. Acad. Sci.*, 2021, **118**, e2107632118.
77 L. A. Wilen, J. S. Wettlaufer, M. Elbaum and M. Schick, *Phys. Rev. B: Condens. Matter Mater. Phys.*, 1995, **52**, 12426–12433.
78 J. S. Wettlaufer, *Phys. Rev. Lett.*, 1999, **82**, 2516–2519.
79 P. Parashar, K. V. Shajesh, K. A. Milton, D. F. Parsons, I. Brevik and M. Boström, *Phys. Rev. Res.*, 2019, **1**, 033210.
80 K. A. Milton, *J. Phys. A*, 2004, **37**, R209–277.
81 W. C. Chew, *Waves and Fields in Inhomogeneous Media*, IEEE, 1995.

